NANOCRYSTALLIZATION IN MARGINAL GLASS FORMING ALLOYS

A THESIS SUBMITTED TO
THE GRADUATE SCHOOL OF NATURAL AND APPLIED SCIENCES
OF
MIDDLE EAST TECHNICAL UNIVERSITY

BY

TUBA DEMİRTAŞ

IN PARTIAL FULFILLMENT OF THE REQUIREMENTS
FOR
THE DEGREE OF MASTER OF SCIENCE
IN
METALLURGICAL AND MATERIALS ENGINEERING

JANUARY 2013

Approval of the thesis:

NANOCRYSTALLIZATION IN MARGINAL GLASS FORMING ALLOYS

submitted by **TUBA DEMİRTAŞ** in partial fulfillment of the requirements for the degree of **Master of Science in Metallurgical and Materials Engineering Department, Middle East Technical University** by,

Prof. Dr. Canan ÖZGEN   _____
Dean, Graduate School of **Natural and Applied Sciences**

Prof. Dr. C. Hakan GÜR   _____
Head of Department, **Metallurgical and Materials Engineering**

Assist. Prof. Dr. Yunus Eren KALAY   _____
Supervisor, **Metallurgical and Materials Eng. Dept., METU**

Examining Committee Members:

Prof. Dr. Tayfur ÖZTÜRK   _____
Metallurgical and Materials Eng. Dept., METU

Assist. Prof. Dr. Yunus Eren KALAY   _____
Metallurgical and Materials Eng. Dept., METU

Prof. Dr. M. Vedat AKDENİZ   _____
Metallurgical and Materials Eng. Dept., METU

Prof. Dr. M. Kadri AYDINOL   _____
Metallurgical and Materials Eng. Dept., METU

Prof. Dr. Raşit TURAN   _____
Physics Dept., METU

Date: 31.01.2013

I hereby declare that all information in this document has been obtained and presented in accordance with academic rules and ethical conduct. I also declare that, as required by these rules and conduct, I have fully cited and referenced all material and results that are not original to this work.

Name, Last Name: Tuba DEMİRTAŞ

Signature   :

ABSTRACT

NANOCRYSTALLIZATION IN MARGINAL GLASS FORMING ALLOYS

Demirtaş, Tuba

M. Sc., Department of Metallurgical and Materials Engineering

Supervisor: Assist. Prof. Dr. Yunus Eren Kalay

January 2013, 68 Pages

The marginal glass-forming alloys have attracted much attention due to unique products of devitrification with a very high number density of nuclei up to 10^{23}m^{-3}. Among these alloy systems, utmost interest is given to Al-RE and Al-TM-RE alloys with excellent lightweight mechanical (fracture strength close to 1 GPa) and chemical properties attributed to the presence of an extremely high density of nanocrystals embedded in an amorphous matrix. Classical nucleation theory fails in explaining this abnormal nucleation behavior, several other mechanisms have been proposed; however, there is still no agreement on the exact nucleation mechanism. Al-Tb system was investigated in liquid and solid amorphous states with a collective study of ab-initio MD and RMC simulations and state of art X-rays and e-beam techniques. Regions of pure Al clusters in the solid and liquid states were detected with the sizes extending up to 1-2 nm length. Al clusters interconnecting regions lead to formation of RE rich MRO structure which gave rise to the pre-peak in S(Q)-Q data in liquid and solid states. Specimens having MRO were crystallized within a controlled atmosphere and temperature and investigated using a combined study of TEM, HRTEM, SEM, XRD and DSC. HRTEM investigations and JMA results indicated different mechanism of nucleation. Therefore the kinetics of highly populated nuclei formation was found too complicated to be explained by well-known JMA approach. Mechanical tests were applied to determine the effects of morphology and populations of nanocrystals embedded in amorphous matrix. The tensile tests and the subsequent fracture surface analysis indicated brittle type of failure and the formation of shear bands, respectively. Relatively high hardness and tensile strength were detected by nanocrystallization.

Keywords: nanocrystallization, medium-range order, electron microscopy, synchrotron X-ray, mechanical properties

ÖZ

MARJİNAL CAMSI METALLERDE NANOKRİSTAL OLUŞUMU

Demirtaş, Tuba

Yüksek Lisans, Metalurji ve Malzeme Mühendisliği Bölümü

Tez Yöneticisi: Yrd. Doç. Dr. Yunus Eren Kalay

Ocak 2013, 68 Sayfa

Marjinal camsı metal alaşımları, $10^{23} m^{-3}$ oranlarına ulaşan yüksek sayısal çekirdek yoğunluğuna sahip özgün devitrifikasyon ürünleri nedeniyle oldukça ilgi çekmektedirler. Amorf matris içinde gömülü bulunan yüksek sayısal yoğunluktaki nanokristallerin varlığına bağlı olarak gelişen hafiflik, mekanik (1 GPa değerine yakın kırılma dayancı) ve kimyasal özellikler nedeniyle, bu camsı metal alaşımları arasında en büyük ilgi Al-RE ve Al-TM-RE alaşımlarına gösterilmektedir. Klasik çekirdeklenme teorisi bu anormal çekirdeklenme mekanizmasını açıklayamamaktadır ve halihazırda önerilmiş olan çeşitli mekanizmalar üzerinde ise, henüz bir anlaşmaya varılamamıştır. Bu projede Al-Tb alaşımı sıvı eriyik ve katı amorf hallerinde ab-inito MD ve RMC simülasyonları ile ileri X-ışınları ve elektron demeti teknikleriyle incelenmiştir. Bu çalışmalar sonucu sıvı ve katı hallerde 1-2 nm uzunluğunda saf Al MRO bölgeleri tespit edilmiş ve ara bölgelerde S(Q)-Q verilerinde ön-pik oluşumunu doğuran RE açısından zengin orta-erimli düzene sahip yapıların oluştuğu görülmüştür. Bu şekilde MRO içeren amorf yapılar kontrollü atmosfer altında kristallendirilmiş ve TEM, HRTEM, SEM, XRD ve DSC ortak çalışmaları ile incelenmiştir. HRTEM ve JMA ile gerçekleştirilen kinetik analiz sonuçları farklı çekirdeklenme mekanizmalarını işaret etmiş ve bunun sonucu olarak JMA yönteminin tek başına bu mekanizmayı açıklamada yeterli olmayacağı öngörülmüştür. Amorf yapı içindeki nanokristallerin morfoloji ve popülasyonunun mekanik özelliklere etkisi çalışma kapsamında incelenmiştir. Çekme testleri ve takiben yapılan kırılma yüzeyi analizleri, gevrek kırılma sonucunu ve kesme kuşağı oluşumunu ortaya koymuştur. Nanokristallenme ile, nispeten daha yüksek sertlik ve çekme dayanımı değerleri saptanmıştır.

Anahtar kelimeler: nanokristalleşme, kristal ara geçiş formları, elektron mikroskobu, synchrotron X-ışını, mekanik özellikler

To My Precious Family…

ACKNOWLEDGEMENTS

TABLE OF CONTENTS

LIST OF TABLES

TABLES

LIST OF FIGURES

FIGURES

NOMENCLATURE

APT: Atom Probe Tomography

BF: Bright Field

BMG: Bulk Metallic Glass

CCD: Charge Coupled Device

CN: Coordination Number

CNA: Common Neighbor Analysis

DSC: Differential Scanning Calorimetry

ECAP: Equal Channel Angular Pressing

EXAFS: X-ray Absorption Fine Structure

FCC: Face Centered Cubic

FEM: Fluctuation Electron Microscopy

FFT: Fast Fourier Transform

$g(r)$: Pair Correlation Function

GGA: Generalized Gradient Approximation

H – A: Honeycutt-Anderson

HEXRD: High Energy Synchrotron X-ray Diffraction

HRTEM: High Resolution Transmission Electron Microscopy

JMA: Johnson-Mehl-Avrami

LDA: Local Density Approximation

LRO: Long Range Order

MD: Molecular Dynamics

MGF: Marginal Glass Former

MRO: Medium Range Order

MUCAT: Midwest Universities Collaborative Access Team

PAW: Projector Augmented Wave

PCF: Pair Correlation Function

PDF: Pair Distribution Function

RE: Rare Earth Elements

RMC: Reverse Monte Carlo

S(Q): Structure Factor Function

SAED: Selected Area Electron Diffraction

SAS: Small Angle Scattering

SEM: Scanning Electron Microscopy

SRO: Short Range Order

STZ: Shear Transformation Zone

TEM: Transmission Electron Microscopy

TM: Transition Metal

TTT: Time Temperature Transformation

XANES: X-ray Absorption Near Edge Structure

XRD: X-ray Diffraction

VASP: Vienna Ab-initio Simulation Package

VP: Voronoi Polyhedra

CHAPTER 1

INTRODUCTION

1.1. History of Metallic Glasses

Metallic glasses have been recognized as one of the most exciting materials of 21st century. The appealing properties of metallic glasses come from the non-traditional arrangement of atoms having random configurations even at room temperature. This non-crystalline structure provides futuristic wide range of applications from aerospace and defense industries to daily used products.

The basic production technique of metallic glasses consists of quenching liquid alloy to room temperature. If the quench rate is sufficiently high enough, a disordered structure similar to liquid is expected. Traditionally, quenching was performed using water and oil. However, the gaseous layer formed between the alloy and quenching media limits the heat transfer, decreases the cooling rate and causes the crystallization of the molten alloy. The inefficiency of quenching into liquid media was firstly noticed by a research group at Caltech. W. Klement, Williens and Duwez [1]. They used a cold metal plate instead of liquid media in order to provide a fully metal-metal contact and increase the cooling rate by fast thermal conduction. This technique, so-called as splat quench, provides cooling rates much faster than 10^6 K/s. The very first metallic alloy provided by this procedure was $Au_{75}Si_{25}$ alloy [1-2]. Following this study several new metallic systems have been discovered by various rapid solidification and mechanical deformation techniques. Some of the major achievement in the field is summarized in Table 1.1.

1.2. Thermodynamic and Kinetic Properties of Metallic Glasses

The mystery of producing metallic glasses relies on a critical cooling rate upon which the nucleation of any crystal structures is suppressed. Upon relatively large cooling rates, liquid metals do not crystallize at their nominal freezing but instead they are highly undercooled. Such undercoolings of the metallic alloys below the liquidus temperature causes a slowdown in the kinetics because of the increased viscosity. In general, an undercooled liquid should reach a viscosity of $\sim 10^{12}$ Pa s to become a glass [9-10]. The melting point viscosity of metallic glasses is 10^{-2}-10^{-1} Pa s when it is 10^{-3} Pa s for normal liquids [10].

Table 1.1 Some important developments in the field of metallic glass.

Year	Achievement	Reference
1960	First metallic glass alloy ($Au_{75}Si_{25}$) produced by Duwez et al.	[1]
1976	Melt-spinning technique was dicovered by Liebermann and Graham.	[3]
1981	First Al based amorphous alloy (Al-Fe-B and Al-Co-B) was produced by Inoue et al.	[4]
1998	First application of metallic glass (Vitreloy) was on golf clubs	[5]
1996	$Zr_{41.2}Ti_{13.8}Cu_{12.5}Ni_{10}Be_{22.5}$ metallic glass was produced at a cooling rate ~1K/s.	[6]
2004	First bulk amorphous steel was produced by two different research groups (Oak Ridge National Laboratory and University of Virginia)	[7-8]

The viscosity of a metallic glass is gained by the drastic increase in the driving force for crystallization (ΔG), when the temperature of the liquid was taken under the liquidus temperature. The increase of driving force pushes the metal into a non-equilibrium state. The relation between the viscosity and temperature is given by the formula:

$$\eta = \eta_0 \exp (W/kT) \qquad\qquad \text{Equation 1.1}$$

where η_0 is the viscosity limit at high temperature, W is the activation energy and k is the Boltzmann constant [11]. As it is given by the formula, the increase of viscosity with decreasing temperature is exponential. In addition to that, there is an expectation of linearity between log (η) and log (1/T) with an assumption of W being independent of temperature. However, this is not meaningful for metallic glasses because of the significant increase in viscosity with supercooling [11]. Figure 1.1 shows the schematics of basic glass formation procedure. In order to obtain an amorphous structure, material should be cooled very fast to suppress the formation of any long range order. By cooling below the melting temperature in a fast manner that prevents the nucleation and growth of any crystalline phase, a frozen liquid and amorphous structure is obtained due to the drastic increase in viscosity.
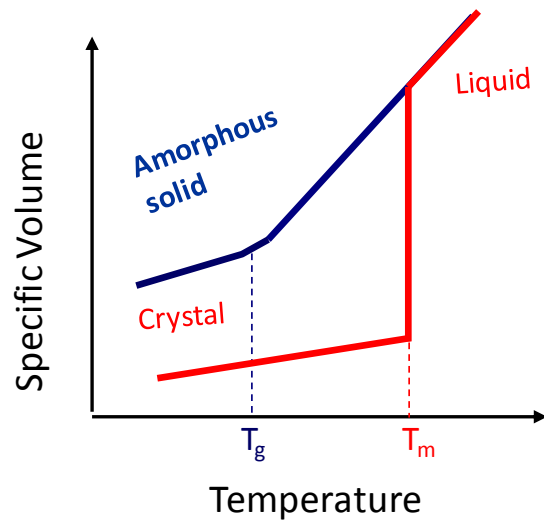
Figure 1.1. The specific volume versus temperature diagram showing amorphous solid formation.

Since the formation of metallic glasses depends on the cooling rate of solidification, the vitrification process can be also explained by conventional time-temperature-transformation (TTT) diagram. Figure 1.2 shows a typical TTT for metallic glass formation upon solidification. With decreasing temperature, both of increasing viscosity and increasing free energy (driving force) determines the crystallization rate in a supercooled liquid. As this two has opposite effects, the resultant TTT diagram occurs as a typical nose-shaped scale. In order to have a good glass forming ability the diagram should be shifted to right or the supercooled region should be narrowed [11-12].

Although cooling rate is a key parameter in vitrification, it is not enough to predict the vitrification capability of metallic alloy systems. Since the first metallic glass was discovered, several empirical rules have been postulated to define glass forming ability. Some of the fundamental rules are summarized below [11,13]:

- Systems need more than three elements,
- Atomic size difference exceeding 12% among main constituents,
- Negative heat of mixing among main constituents

The combination of cooling rate requirements and empirical rules for amorphous phase formation results in two broad categories of metallic glasses. The first type is called as bulk metallic glasses (BMG) and the second one is marginal glass forming (MGF) alloys. The fundamental difference between these categories is the required critical cooling rate. The BMGs are required 10^2 K/s on the other hand for MGFs much higher cooling rates on the order of 10^6 K/s is essential [11].

3
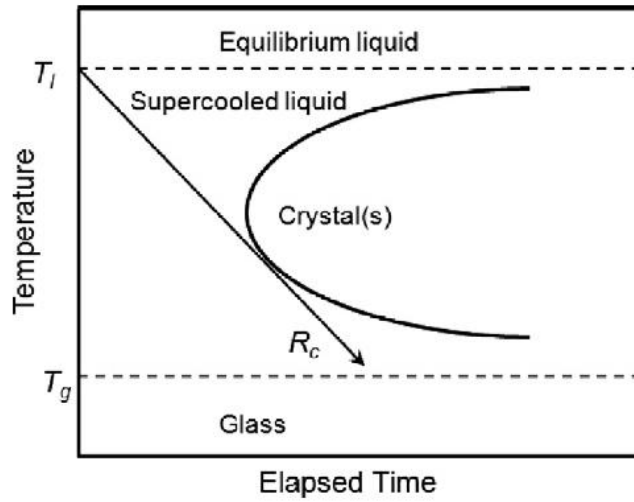
Figure 1.2. The TTT diagram of a metallic glasses with the representative critical cooling rate (R_c). Adopted from [11].

The as-solidified structures and their devitrification products may show fundamental differences as explained in the following sections. Examples of BMG and MGF are given in Table 1.2.

Table 1.2. Examples of BMG and MGF.

Bulk Metallic Glasses	Marginal Glass Formers
Vitreloy 1 ($Zr_{41.2}Ti_{13.8}Cu_{12.5}Ni_{10}Be_{22.5}$) [12]	Finemet ($Fe_{73.5}Cu_1Nb_3Si_{13.5}B_9$) [14]
$Pd_{40}Ni_{40}P_{20}$ [12]	Nanoperm ($Fe_{84}Zr_{3.5}Nb_{3.5}B_8Cu_1$) [14]
$Zr_{65}Al_{7.5}Ni_{10}Cu_{17.5}$ [12]	$Fe_{82.3}Nd_{11.8}B_{5.9}$ [14]
$Pd_{40}Cu_{30}Ni_{10}P_{20}$ [13]	Al-RE-TM [14]
$Zr_{55}Ti_5Al_{10}Cu_{20}Ni_{10}$ [13]	Al-RE [14]

1.3. Structure of Metallic Glasses

Metallic glasses are the materials that do not possess long range order within the structure as the ordinary crystalline metals. Therefore, the classification and structural explanation of metallic glasses can not be extended by standard crystal lattice theory. The structural difference between a crystalline and amorphous metallic alloy can be easily detected by a simple X-ray diffraction scan. Figure 1.3 shows typical XRD patterns for crystalline and amorphous metallic systems.
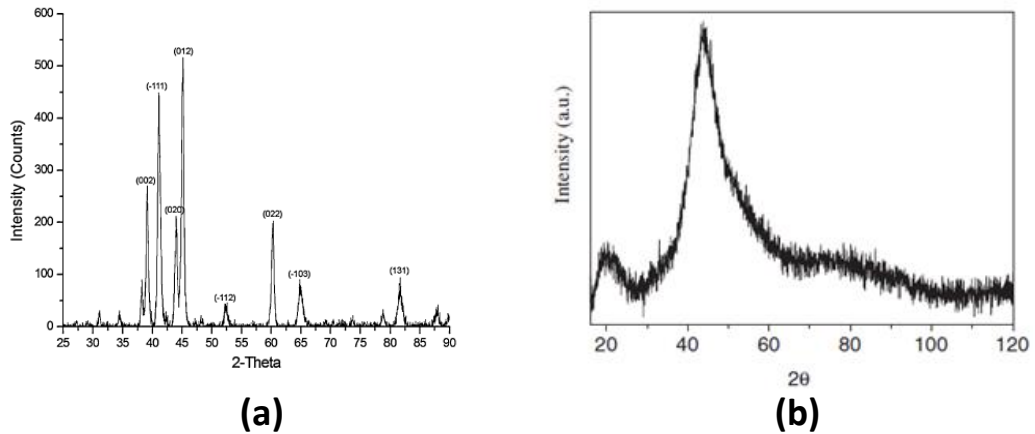
Figure 1.3. XRD patterns of (a) martensitic NiTi shape memory ribbon adopted from [15] (b) the $Al_{87}Ni_7Nd_6$ as-quenched alloy adopted from [10].

XRD of crystalline structure consists of systematic Bragg reflections indicating long-range atomic configurations on the other hand metallic glass can only persist short or medium range order so they lack any diffraction lines. The schematic of crystalline and SRO atomic configurations are shown in Figure 1.4. The SRO nearest-neighbor arrangements are qualitatively similar for each atom however they do not repeat themselves upon appreciable distances.
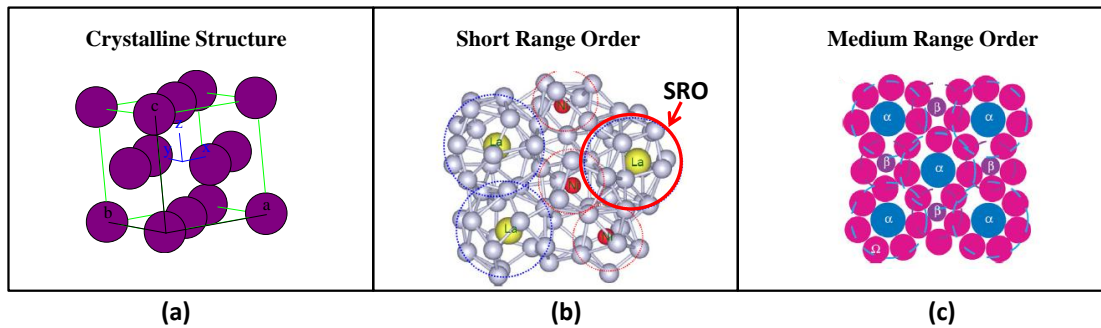
Figure 1.4 Schematic view of (a) crystalline structure (fcc-Al), (b) SRO adopted from [11] and (c) MRO adopted from [16] respectively.

Some parameters such as pair distribution function (PDF) and structure factor S(Q) are commonly used to describe the internal short range order (or disorder). Pair distribution function is the probability index of atomic distributions around a selected center atom with respect to a distance r [11, 17]. An example of PDF is shown in Figure 1.5. In general, the first peak in PDF curve indicates the atomic distribution of nearest neighbor shell which shows the distance of short range order. The further distance in the same curve up to 1-2nm is excepted as the keyword of medium range ordered structure which has neither short nor long range order [11]. The number of atoms that exists around this selected center atom is

5

called the coordination number (CN) and it can be easily determined from the g(r)-r curves indeed.
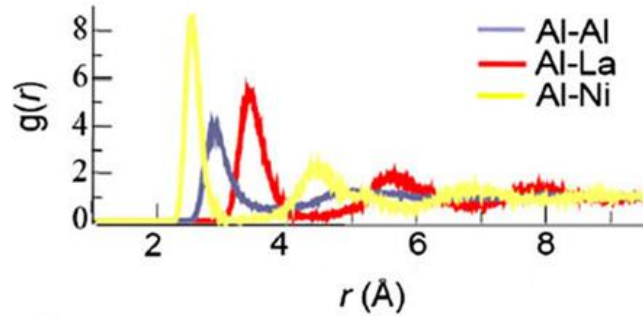
Figure 1.5 PDF of Cu (liquid) at 1500 K obtained from molecular dynamics simulations. Adopted from [18]

Structure factor (S(Q)), can be explained as the Fourier transform of the pair distribution function in reciprocal space [11, 17]. It determines the scattering of incident radiation basically and it can be measured by neutron or X-ray experiments. Total structure function is the summation of all partial structure factors each of that are the Fourier transform of PDFs.

1.4. Structural Characterization of Metallic Glasses

The determination of the chaotic structure in metallic glasses is still an attractive area of research. Researchers approach the disorder structure via various techniques such as XRD, neutron scattering, high energy XRD (HEXRD-synchrotron analysis), X-ray absorption fine structure (EXAFS) and X-ray absorption near edge structure (XANES), transmission electron microscope (TEM), high resolution TEM, fluctuation electron microscope (FEM) and atom probe tomography (APT). Most common method is using combination of different techniques and constructing a related path of analysis by the techniques listed above under a straight correlation. A brief summary of each technique to investigate the disordered structure is given below.

1.4.1 X-Ray Diffraction

XRD is the heading method in determination of the unknown internal structures. It is basically used to determine the atomic and molecular distributions in crystalline structures. X-rays are used in obtaining a diffraction pattern by Bragg's Law which is:

$$2dsin\theta = n\lambda \qquad\qquad\qquad \text{Equation 1.2}$$

where d is the plane spacing, θ is incident angle and λ is the wavelength. Since the SRO or MRO in amorphous structures lack any diffraction line because of no atomic order distribution, amorphous structures usually exhibit a main wide peak with following

6

uncertain shoulders [11, 17]. The typical XRD pattern of an amorphous metal was shown in Figure 1.3(b).

1.4.2 Neutron Scattering

Neutron scattering and the X-ray diffraction both rely on the same basis. In each method, the scattering is related to the total structure factor that includes the atomic scattering factors (f). At this point, the difference between neutron scattering and XRD comes out by means of the variable in reciprocal space (q) dependence of f. Since the scatterer is atomic nucleus for neutrons, the scattering factor is independent of q when the XRD scatterer (electron clouds) presents the q dependence [17].

In both X-ray and neutron scattering methods, the small angle scattering (SAS) technique is also used to reach the larger scale investigations. By using SAS, it is possible to investigate the scales higher than 10Å nearly up to thousands of angstroms [19]. In larger scales, SAS strongly provides the detection of any structural information on the random arranged systems as metallic glasses. As an example to comparison of neutron diffraction and X-ray diffraction, the powder diffraction patterns of intermetallic $CeRhGe_3$ given in Figure 1.6.
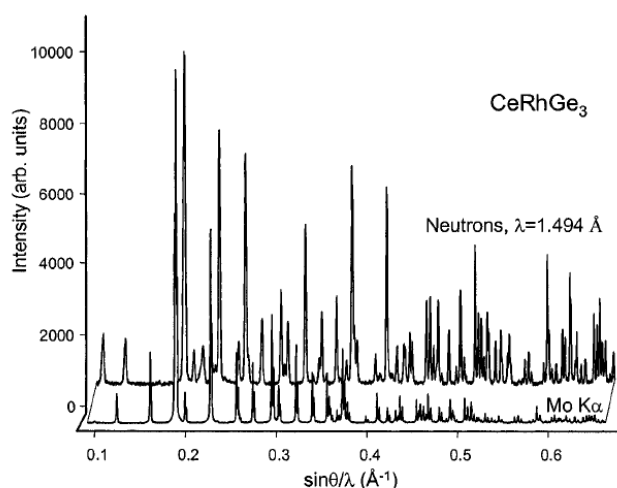
Figure 1.6 Two powder diffraction patterns of intermetallic $CeRhGe_3$ showing Mo-Kα X-ray data radiation at room temperature (bottom plot) and neutron diffraction data at T=200 K (top plot with λ of thermal neutrons is 1.494 Å). Adopted from [20].

1.4.3 Synchrotron Resolution

HEXRD synchrotron facilities offer significantly high intensity and short-adjustable wavelength which lead to obtain further structural details. [17, 21].

Synchrotron facility is a world-wide particle accelerator that can be used to produce white or monochromatic beam with the help of a single-crystal monochromator. It is generally the best way to gain high collimation, high and accurate resolution and perform a controlled

alignment during structural investigations with X-rays. A schematic distribution of HEXRD synchrotron pattern is given in Figure 1.7.
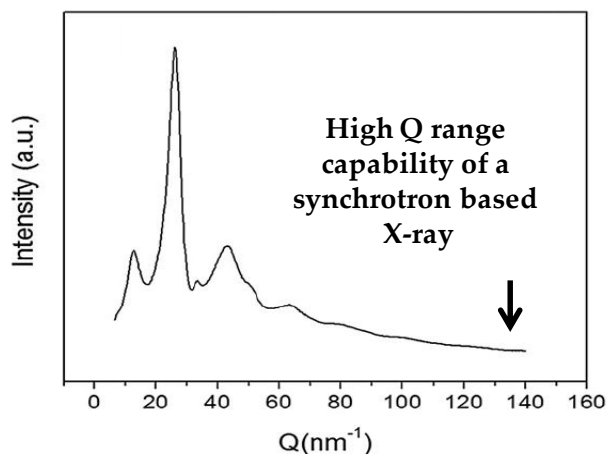
Figure 1.7 HEXRD synchrotron diffraction pattern of as-quenched $Al_{90}Sm_{10}$ alloy Adopted from [22].

1.4.4 Extended X-ray Absorption Fine Structure and X-ray Absorption Near Edge Structure

The X-ray absorption fine structure (XAFS) is another common method of defining the unknown structures. The method also provides extended X-ray absorption fine structure (EXAFS) and X-ray absorption near edge structure (XANES) [11]. XAFS are important on the energy resolved and element specific absorption coefficient determinations. It is also used to determine the local chemistry around a specific element. When dealing with XANES, it is found to be difficult to comment on results, but the ab-initio calculations are used to predict the resultant data with the description of local electronic area of atomic clusters [11]. The schematic distribution of EXAFS and XANES are shown in Figure 1.8.
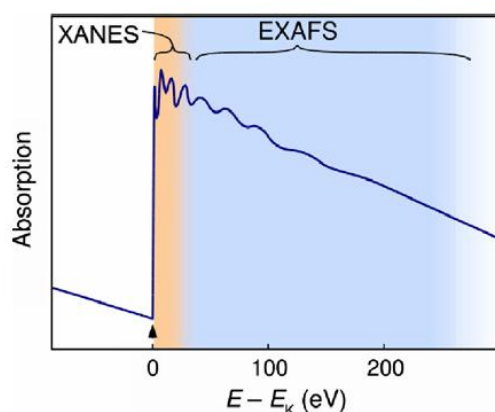
Figure 1.8. A schematic view of X-ray absorption spectrum with XANES and EXAFS included. Adopted from [11].

1.4.5 Transmission Electron Microscopy

Transmission electron microscopy is a leading method used in structural investigations. TEM method strongly used in checking the degree of vitrification after rapid cooling and detecting the nanoscale devitrification products.

HRTEM provides atomic level analysis in 2D scale in real space and the reciprocal space with the implemented fast Fourier Analysis capability. The selected area electron diffraction (SAED) technique in TEM analysis also provides higher energy levels of diffraction with a better resolution of the structure when compared to ordinary XRD [11]. The TEM micrographs with inserted SAED patterns of a crystal and amorphous structure are shown in Figure 1.9(a) and (b).

(a) **(b)**
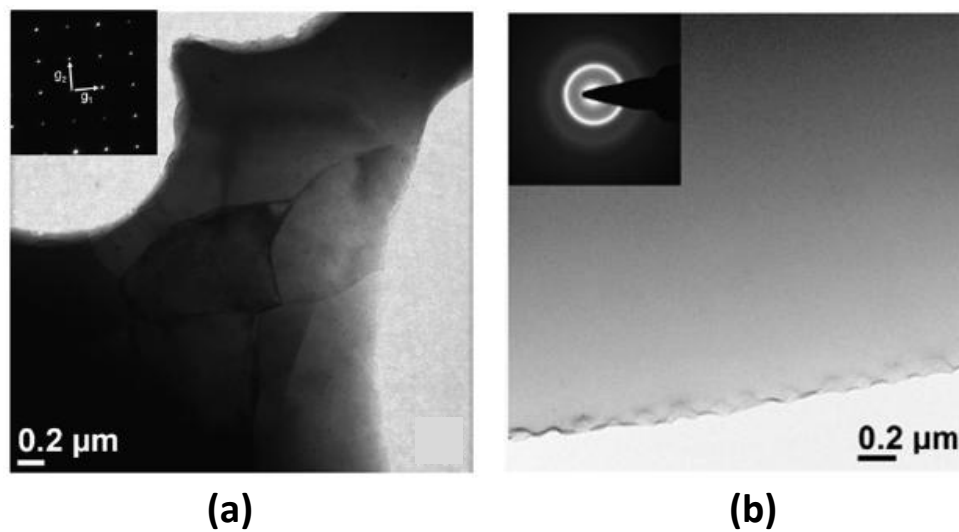
Figure 1.9. TEM micrographs of (a) crystalline and (b) amorphous structures in $Al_{90}Sm_{10}$ alloy with inserted SAED patterns. Adopted from [22].

1.4.6 Fluctuation Electron Microscopy

FEM has been recently become a powerful tool in determination of MRO in amorphous matrix. By the nanometer sized X-ray or electron beam, FEM method scans the surface of the sample to measure the fluctuations in intensity of scattering that provides the detection of any medium ranged ordering over the sample [23].

As shown in Figure 1.10, electron beam scanned over a MRO region results in enhanced speckles from the ordered coherent atomic correlations. The variance in speckle intensities with respect to reciprocal space vector gives the insights of configuration in MRO structure.
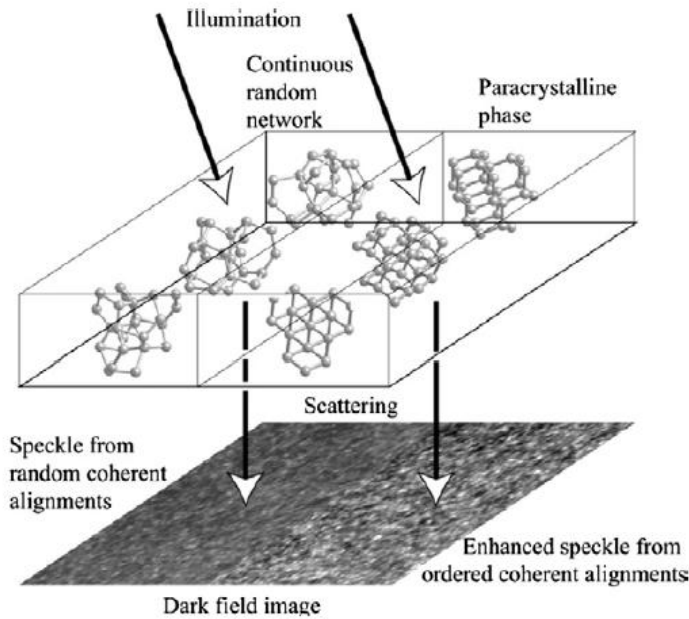
Figure 1.10. Working principle of FEM analysis. Adopted from [11, 24].

1.4.7 Atom Probe Tomography

Another useful method, the APT, gives a topological point of view with atomic chemical resolution. Basically, APT defines the local positions of atoms with a position-sensitive detector [25-26]. There exists two main mechanisms in working principle of an APT that are the field ionization and field evaporation [25]. APT technique provides 2D concentration maps of the alloys which can be transformed into 3D tomography data views [25-26] to observe the atomic distribution over a specific direction. These suggest the clustering and ordering mechanisms inside the unknown structure in a preferred visual scale. An example for clustering in a marginal glass former, $Al_{90}Sm_{10}$ is shown Figure 1.11.
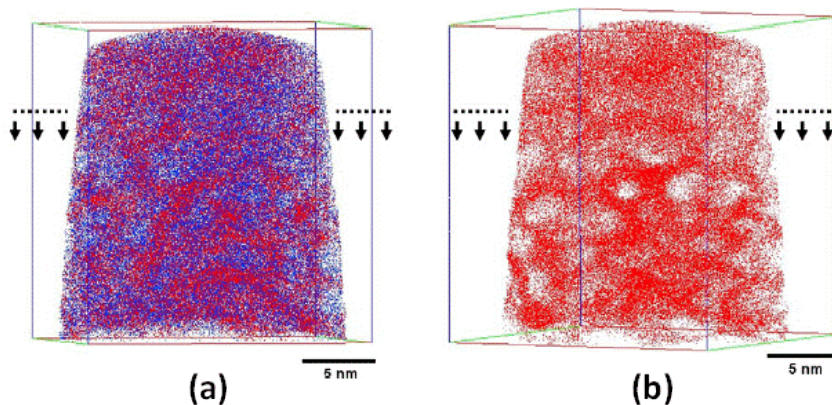
Figure 1.11. APT results of $Al_{90}Sm_{10}$ alloy, showing (a) Al atoms in blue and Sm atoms in red and (b) Sm atoms only. Adopted from [27].

In this study XRD, HEXRD, TEM are HRTEM are used as the basic structural characterization tools. Results of previous APT studies [26] are also implemented to recent findings.

1.5. Atomic Simulations of Metallic Glasses

Several atomic simulation techniques have been implemented to metallic glass systems in order to get insights of most accurate three dimensional distributions of atoms in the as-quenched state. Among these, ab-initio molecular dynamics (MD) analysis is the leading method in determination of the differences inside the amorphous structure. Ab-initio MD basically reveals the interatomic interactions and electronic structures of the material. Accuracy in energy, force and dynamic process is the promising characteristic of the analysis if it is done appropriately. Although ab-initio MD is a powerful technique, there also exists some significant handicaps of ab-initio method. First of all, the modeling can not be done for all materials and this mostly narrows down the area of usage. In order to calibrate the problem of exchange-correlation energy determination, local density approximation (LDA) and generalized gradient approximation (GGA) are included in commonly used methods. Another problem is the lack of representing all material properties. There are only restricted number of parameters which can be modeled by ab-initio MD simulations [11].

Since the simulation time of ab-initio MD analysis is very short as ~ps, the distance between atoms becomes less than ~1nm. This prevents the structural order and creates a representative accuracy during analysis. Also the ab-inito MD analysis can be done only ~100 atoms that results in an advantage of having few alloying in the box [11]. But also, these 100 atomic box results in a representative default since the real case does not composed of only 100 atoms in any alloying condition. The distribution of atoms according to the interatomic potentials and such properties inside of this volume is gained by the ab-initio MD programs as Vienna Ab-initio Simulation Package (VASP) [28-31].

Since, the real conditions includes different volumes with higher number of atoms, the simulation sequence continues with another computational package the Reverse Monte Carlo (RMC) modeling [32]. The method is a structural modeling technique based on experimental data [32] used to catch an atomic configuration that represents the real material and it becomes widely used in research of structure in metallic glasses in recent years [11]. RMC method requires basically the following iteration steps: random movement of the atoms to simulate the configurational space, calculation of energy term (the difference between structural parameters of the trial and target configurations), determining the fit residue and finally comparing this fit residue with the previous one [11, 32].

Since RMC method is a trial and error method, the results requires accurate determinations and a correlated study with experimental and computational analysis. RMC analysis provides random distributions of previously created atomic configurations. Therefore, RMC method tries to reach the perfect fit with experimental data only in topological manner. The lack of kinetic base in RMC [11] method leads to a need of a collective study of ab-initio MD, experimental results and RMC analysis. In light of this requirement, a schematic example of RMC curve compared with real experiment data shown in Figure 1.12

The long-range order distribution is lacking in amorphous systems. Therefore some sophisticated structural analysis technique has been implemented in disordered systems to represent the short and medium range topological and chemical order. Among these approaches, Voronoi Tessellation, Honeycutt-Anderson, and Warren-Cowley analysis are widely used.
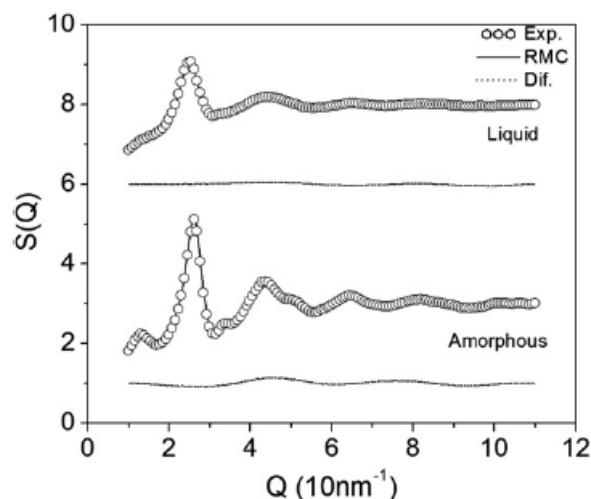
Figure 1.12 Total structure function and the fitted RMC curve shown for as-quenched and liquid $Al_{89}Sm_{11}$ at 1313K. Adopted from [33].

1.5.1 Voronoi Analysis

The RMC provides the structural match between calculated and experimental methods, but only in two dimensional projections. Voronoi Tessellation is commonly used in order to get a successful long range ordered three dimensional distribution of atoms. Voronoi Tessellation is mainly used to divide the three dimensional space into cluster-like areas centered by each atom. Method allows the determination of the coordination number by selecting the closest atoms to the center atom without dealing with the other parts of the space [11, 33]. The schematic explanation of this method is given in Appendix 1.

1.5.2 Honeycutt-Anderson Index

Honeycutt-Anderson (H – A) is quite similar to Voronoi's approach in terms of indexing [11, 34]. In H – A index there exists four digits $ijkl$ in which i serves for identifying the bonding of two given atoms, j represents number of nearest neighbors shared by this two atoms, k is the number of bonds and l helps in case of first three numbers being the same when bond geometries are different [11].

1.5.3 Warren-Cowley Parameter

In order to determine the local chemical configurations in unknown structures, Warren – Cowley parameter [11, 35- 36] is widely used in metallic glasses [11]. The chemical short range order is determined by calculating the Warren-Cowley parameter and observing the

distribution of it over the structure. Determination of Warren-Cowley parameter is conducted by

$$\alpha_{AB} = 1 - \frac{Z_{AB}}{x_B Z_A}$$ Equation 1.3

where Z_{AB} is the partial B atoms around A (the CN), Z_A is the total CN around A and x_B is the composition of B. The negative α_{AB} means the unlike bonds are preferred when the positive α_{AB} means the like bonds are preferred. If the parameter α_{AB} is close to zero, that means a random solution is obtained [11].

In this study, Voronoi Tessellation and Warren-Cowley parameters were used to determine the local topological and chemical order, respectively.

1.6. Devitrification of Metallic Glasses

Controlled devitrification of metallic glasses is a promising active area of research. The process consists of crystallizing the fully/partially amorphous specimens under controlled atmosphere by isothermal or isochronal heating. In that sense, identification of important thermodynamical temperatures is important. Differential scanning calorimetry (DSC) is a well-known technique to reveal these critical temperatures [37]. Figure 1.13 shows a representative DSC scan from an amorphous metal indicating the glass transition (T_g) and crystallization (T_x) temperatures. The region between T_g and T_x is called as supercooled liquid region where the material structure acts close to a liquid. Since the supercooled region is not in exact thermodynamic equilibrium in metallic glasses, it is described as quasi-equilibrium [11].
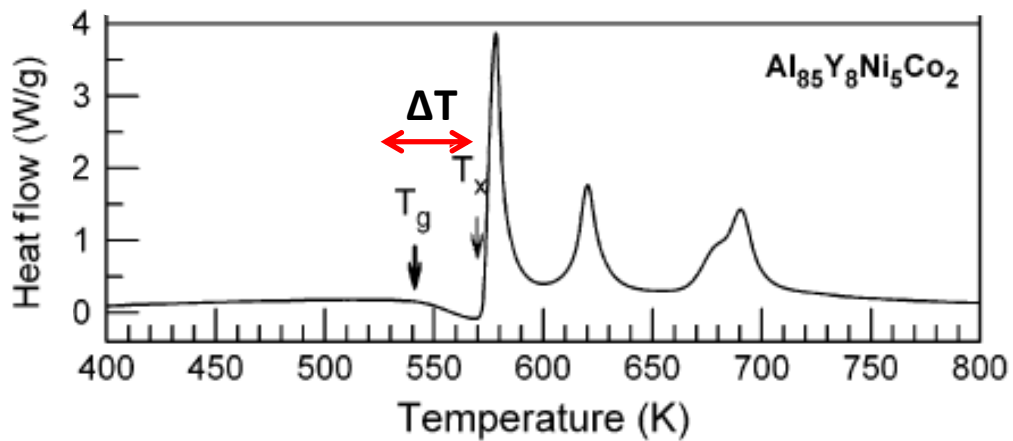
Figure 1.13 The DSC curve of an Al-based BMG heated at 0.67 K/s. Glass transition (T_g), crystallization (T_x) and supercooled liquid region temperatures are shown. Adopted from [38].

1.7. Al-based Metallic Glasses

Among all metallic glasses, Al-based marginal glass formers deserve further attention due to their unusual glass forming ability, extremely high nucleation density upon crystallization and the improved structural and mechanical properties for possible engineering applications.

The group of Al-based metallic glasses is commonly consisted of Al-RE or Al-TM-RE where TM is transition metal and RE is the rare-earth element. Al-RE alloys are taken as the scope of this study mainly due to the simplicity of conducting atomic simulation and producing amorphous alloys. Although, unlike the other metallic glasses Al-RE can be produced as amorphous without alloying with many different elements, it requires high cooling rates to suppress the all crystallization events. A typical vitrification cooling rate of Al-RE is on the order of 10^6 K/s. Melt-spinning is commonly used to reach such high rates of cooling. Some of the significant Al-based compositions and their glass forming ranges are tabulated in Figure 1.14 [4]. Between these binary alloys, Al-Tb is chosen as a model system to study vitrification-devitrification characteristics of Al-RE marginal glass forming alloys. Al-Tb has one of the wider glass forming range yet is has not been studied well in the literature.
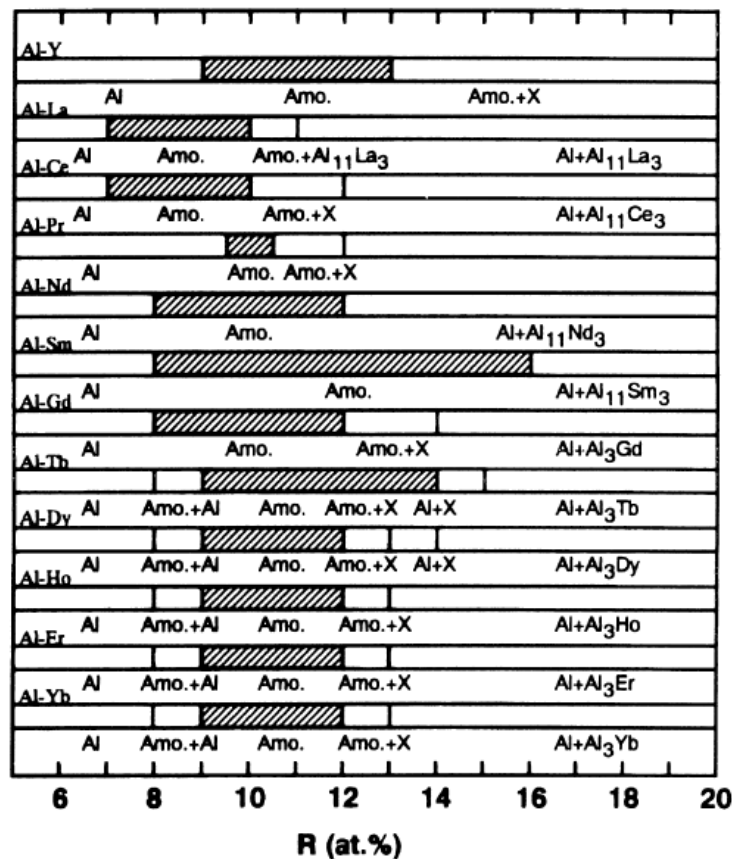
Figure 1.14 Glass forming compositional ranges for Al-RE binary alloys. Adopted from [4].

The same is also true for the thermodynamic properties including the phase diagram. One of the most commonly accepted phase diagram of this system is shown in Figure 1.15 and the composition range studied within this research is marked.

As it was mentioned in the previous sections, the main difference between the bulk metallic and marginal glass forming alloys is the critical cooling rate to produce amorphous structure. This difference may be also affecting the devitrification pathways as there are some variations with their crystallization behaviors. Particularly Fe- and Al-based marginal glass forming alloys devitrifies to a highly populated (10^{20}-10^{24} m^{-3}) nanocrystals of 5-50 nm in size. The glass transition (T_g) and the crystallization (T_x) temperatures of a marginal glass forming alloy most often overlaps so no clear super-cooled liquid regions could ever be observed for these systems. The unique nucleation and growth mechanism causing this enigmatic crystallization pathway has been taken into the consideration of several researchers. Yet there is still no agreement on the mechanism of nucleation.
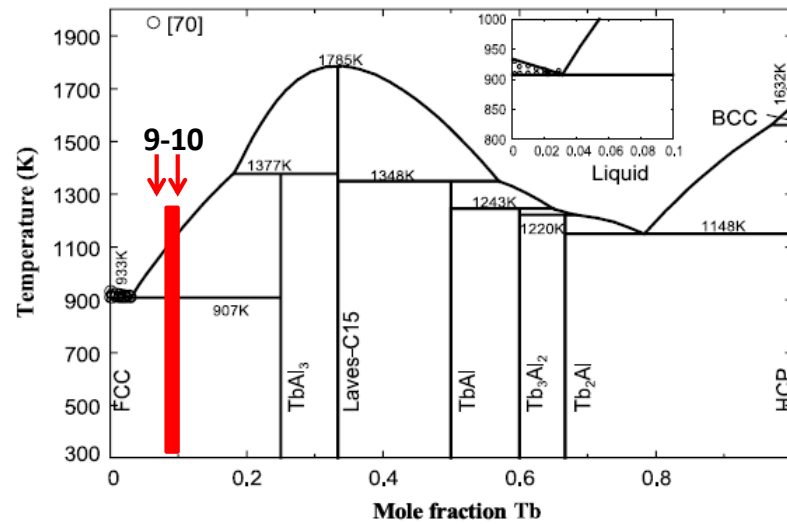
Figure 1.15 Al-Tb phase diagram. The range of compositions studied in this research is highlighted. Adopted from [39].

The previous proposed mechanisms mainly rely on "spinodal decomposition in amorphous state" [40] and "quenched in nucleation" during rapid solidification [41-42]. A relatively new model takes into the consideration of possible medium range order structures existing in liquid state [26, 33]. Detailed information about these approaches will be given in the following chapters. Metallic glasses offer a wide range of engineering applications. Magnets with high energy products, sporting goods, corrosion resistant metals, implants, instruments of surgery, electronic devices are just few examples of metallic glass practices in materials science [12]. In terms of Al based metallic glass, improved mechanical properties comes into prominence [4, 22]. Particularly, the nanocrystalline (nanocrystal + amorphous composites) Al alloys produced by controlled crystallization of Al-metallic glass represents highly driven hardness and tensile strength. These improved mechanical properties make Al-based

15

marginal glass formers a future candidate material to be used in aerospace and defense industry.

Despite the amount of basic research conducted in Al-based metallic glass, a few studies have been conducted to get the insights of engineering applications. Figure 1.16 shows the fracture toughness and hardness values for important Al-RE metallic glass systems. In both case the increase in RE content improves the mechanical properties within the amorphous phase formation range. Beside mechanical properties, corrosion resistance is found to be improved in Al-RE alloys. Table 1 compares the corrosion lost in NaOH and HCl for $Al_{85}Y_{10}Ni_5$, pure Al and AA2024 at room temperature. Under similar testing conditions $Al_{85}Y_{10}Ni_5$ nanocrystalline alloy resisted nor as compared to two other candidates. Therefore, on the light of these preliminary studies it can be surely said that Al-based metallic glasses deserve further attention and consideration.
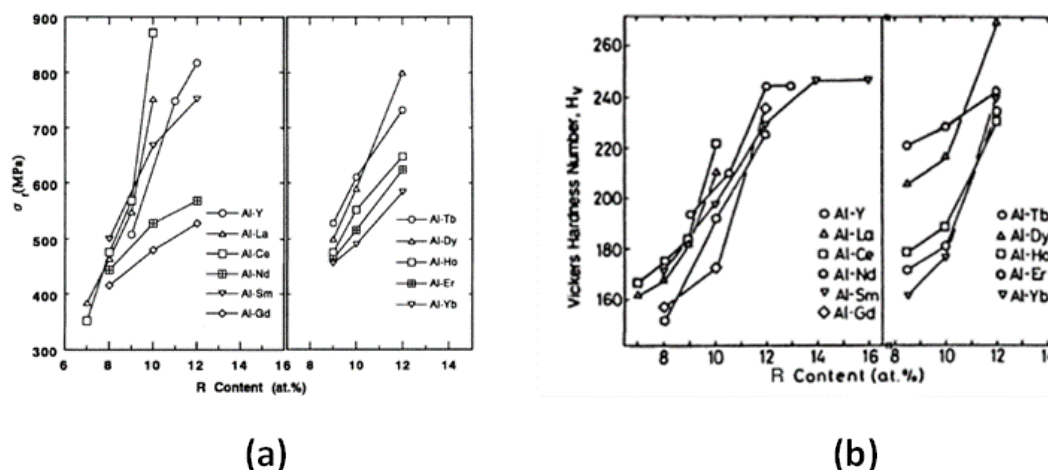
Figure 1.16 The fracture toughness (a) and the hardness (b) values of Al-RE alloys with respect to increasing RE content. Adopted from [4].

Table 1.3. The values of corrosion resistance in years. Adopted from [4]

Alloy	Corrosion Loss (mm/year)	
	In 0.25 M NaOH at 293 K (mm/year)	In 1 M HCl at 293 K
$Al_{85}Y_{10}Ni_5$	2.5	0.055
Al(99.99%)	18.6	0.72
Al-Cu-Mg(2024)	170.0	13.0

1.8. Thesis Organization

The scope of this thesis is to analyze the vitrification and unusual devitrification of Al-RE marginal glass forming alloys by using Al-Tb as a model system. The first chapter of this work summarizes the fundamentals of metallic glasses and gives a notion of important engineering applications of Al-RE metallic glass. In the second part, the as-quenched and liquid structures of $Al_{100-x}Tb_x$ (x = 9, 10) were investigated in details. The amorphous and the molten states were structurally analyzed by high-energy synchrotron X-ray diffraction (HEXRD) correlated Reverse Monte Carlo and ab-initio MD simulations. In the third chapter, this amorphous phase was isothermally crystallized and the nucleation mechanism was revealed by transmission electron microscopy and differential scanning calorimetry experiments. Johnson-Mehl-Avrami type analyses were conducted and compared with the experimental results. In the fourth chapter the emerging mechanical properties were taken into considerations. The tensile and hardness tests were applied and corresponding failure analyses were conducted. In the fifth chapter conclusion was drawn and future recommendations were given.

CHAPTER 2

MEDIUM to LONG RANGE CORRELATIONS in AMORPHOUS and LIQUID STATES OF Al$_{91}$Tb$_9$ ALLOY

2.1. Introduction

Marginal glass forming alloys constitute an important subclass of the metallic glasses mainly due to their unique amorphous structure. Despite to numerous studies on bulk metallic glasses, a few comprehensive studies have been conducted to solve the mind boggling topological and chemical disorder in marginal glass forming metallic alloys. The following chapter will give the insights of the unique atomic structure in amorphous Al$_{91}$Tb$_9$ alloy investigated by complementary state-of-art experimental and computational techniques such as high energy synchrotron X-ray diffraction (HEXRD), transmission electron microscopy (TEM), ab-initio molecular dynamics and reverse Monte Carlo simulations.

2.2. Literature Review

2.2.1 Production of Amorphous Structure in Marginal Glass Former Alloys

One of the fundamental differences between the bulk metallic glasses and marginal glass forming alloys is the critical cooling rate required to suppress the crystallization of any ordered structures. As it was stated in Chapter 1, the critical cooling rate to obtain an amorphous marginal glass forming alloy, is on the order of 10^6 K/second. Such high solidification rates can be only reached by very specific rapid solidification [3, 21] or sputtering [43] techniques. Among the rapid solidification techniques, melt-spinning is the most convenient and efficient method to produce fully amorphous structures [3]. This technique is mainly based on rapid solidification of the molten metal under controlled atmosphere by ejecting it from a nozzle onto a rotating wheel at a very high pressure. The rapid solidification is ensured by the rapid cooling of a long and continuous ribbon shaped alloy via a metal-metal contact on the rotating disc. Generally, ribbons of 10-100 μm thick and 1-2 mm wide can be produced by this technique. The shape and size is usually controlled by nozzle geometry (i.e. flat versus circular geometry) [3].

2.2.2 Atomic structure of Al-RE Marginal Glass Forming Alloy

The controlled crystallization of Al- and Fe-RE based alloys yield a very high number density of nanocrystals with 10-50 nm in diameter. Despite the volume of research in the literature, the mechanism behind this crystallization phenomenon has not explained yet. The

answers of this enigmatic behavior should be hidden within the as-quenched or even in the liquid structure.

Most of the previous studies on Al-RE, Al-RE-TM amorphous atomic structure has focused on Al-Sm alloy. Al-Sm has relatively wider glass-formation range as compared to other Al-RE (Figure 1.12) [4]. One of the first studies on Al-RE belongs to Shiflet et al. who showed that Al-RE may form metallic glass [44, 45]. Following this study, Inoue et al. have been investigated various Al-RE, Al-RE-TM alloy to reveal their glass formation tendencies [4]. Perepezko and Voyles et al. conducted several studies to uncover the true atomic structure of Al-Sm and Al-Y-Fe metallic glasses. In one of their previous studies a cold-rolled and a melt-spun ribbon of $Al_{92}Sm_8$ was produced and investigated under TEM in details [46]. Figure 2.1(a) shows the electron diffraction patterns that measure the short range order (SRO) for as-spun and annealed specimens. The Al <111> peak is not observed when <200> and <220> peaks can be noticed. Most reflections of Al-Sm intermetallic phases are covered by the main broad peak between 0.3-0.4 Å^{-1}. The annealing causing small changes in SRO may explain the shift in <220> peak. Figure 2.1(b) gives the fluctuation electron microscopy (FEM) results from the as-quenched and as-rolled specimens. The as-spun specimen shows the highest FEM signals. The variance (V(k)) close to 0.5 and 0.7 1/Å is close to a pseudo-face centered cubic Al structure.
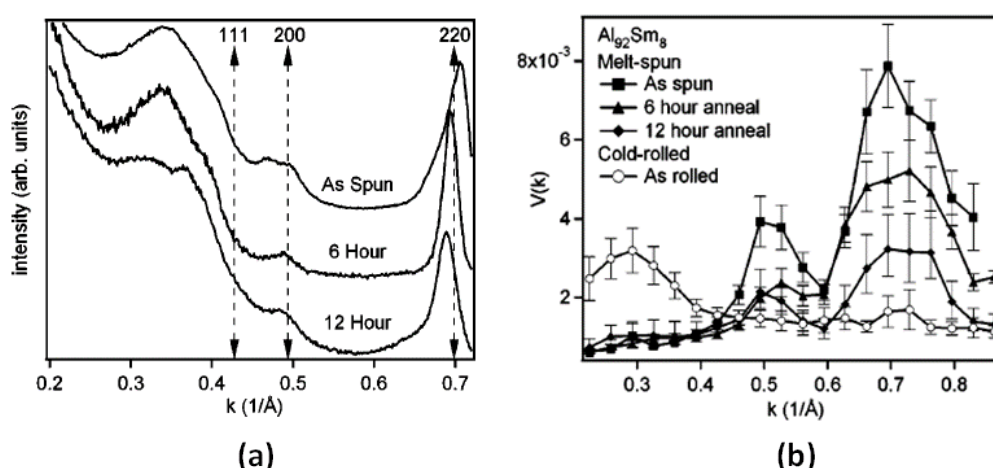
Figure 2.1. FEM results of $Al_{92}Sm_8$ alloy, showing (a) electron diffraction patterns of as-spun, 6h annealed and 12h annealed alloys and the dash lines indicating fcc-Al reflections and (b) variance (V(k)) data for as-spun, 6h annealed, 12h annealed and cold-rolled samples. Adopted from [46].

It should be noted that FEM is sensitive to MRO structure so FEM signals fade as the material crystallites. This is clearly seen for the annealed melt-spun specimens. The FEM signal decreased after 6 and 12 hours annealing. This shows that if any MRO existed in matrix, they transformed to fcc-Al crystals. One interesting observation is the lack of MRO of any pseudo-fcc like structure. On the other hand a relatively strong signal was detected in the low k regime. The authors could not explain the origin of the peak located at 0.3 Å^{-1}.

They have concluded that the fcc like MRO may be related to the nuclei, (so called quenched-in nuclei) that formed during solidification. As shown in Figure 2.2 the highly driven rapid solidification conditions allow those nuclei to form but the growth is restricted by the increase in viscosity.

The amorphous structure of Al-Sm was also investigated by Kalay et al. [21, 22, 27, 33]. HEXRD studies revealed MRO of pseudo fcc-Al and Al-Sm intermetallic like compounds. Particularly, Voronoi type analyses indicated pseudo tetragonal $Al_{11}Sm_3$ configuration in the as-quenched state [33]. This system was also investigated through MD simulations by Wang et al. [47]. Figure 2.3 shows the total and partial pair correlation functions (PCF) for different temperatures. PCF describes the atomic environment around a center atom that is frequently used to determine the SRO. The result of this analysis revealed signatures of tetragonal $Al_{11}Sm_3$ fragments for the temperature close to melting point of $Al_{90}Sm_{10}$ which is in good agreement with Kalay's previous studies [22, 33]. They have also observed a good fraction of fcc and icosahedral SRO in the molten state.
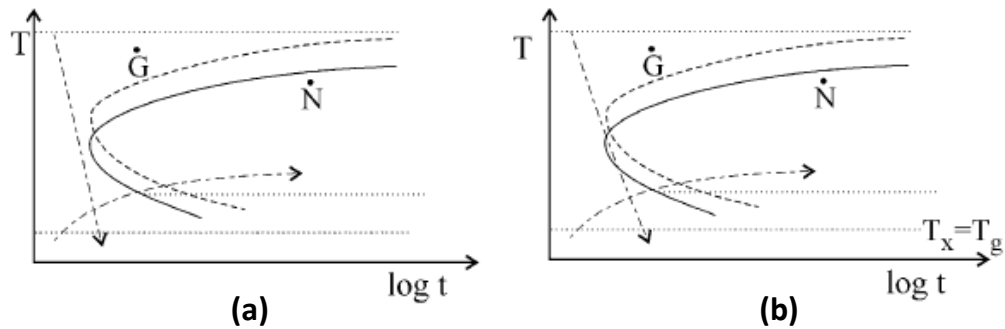
Figure 2.2. Schematic TTT diagrams showing kinetics of (a) nucleation controlled and (b) growth controlled in glass formation. Adopted from [40, 48]

As compared to Al-Sm, there are just a few studies related Al-Tb system. In one of the recent studies by Kalay et al., APT and FEM studies were conducted to resolve the as-quenched structure of $Al_{90}Tb_{10}$. APT analysis revealed regions of pure Al reaching to 1 nm size within the melt-spun $Al_{90}Tb_{10}$ amorphous alloy (Figure 2.4) [26]. This clearly indicates a chemical separation for the as-quenched state. FEM analysis showed these clusters have the tendency of fcc formation. An approximate number density of clusters was calculated as 10^{25} m^{-3} by using APT. It should be noted that the investigated regions are quite small (30x30x4nm) so the representation is relatively weak. On the other hand the spatial resolution in APT is high and it still gives a solid evidence for the existence of topological and chemical ordering in the as-quenched state.

As it is was stated previously, the purpose of this chapter is to analyze the structural order in Al-Tb amorphous alloy. With this motivation, short to medium range correlations in amorphous and liquid $Al_{91}Tb_9$ alloy was investigated in details by using TEM, high energy synchrotron X-ray diffraction, reverse Monte Carlo and ab-initio molecular dynamics simulations.
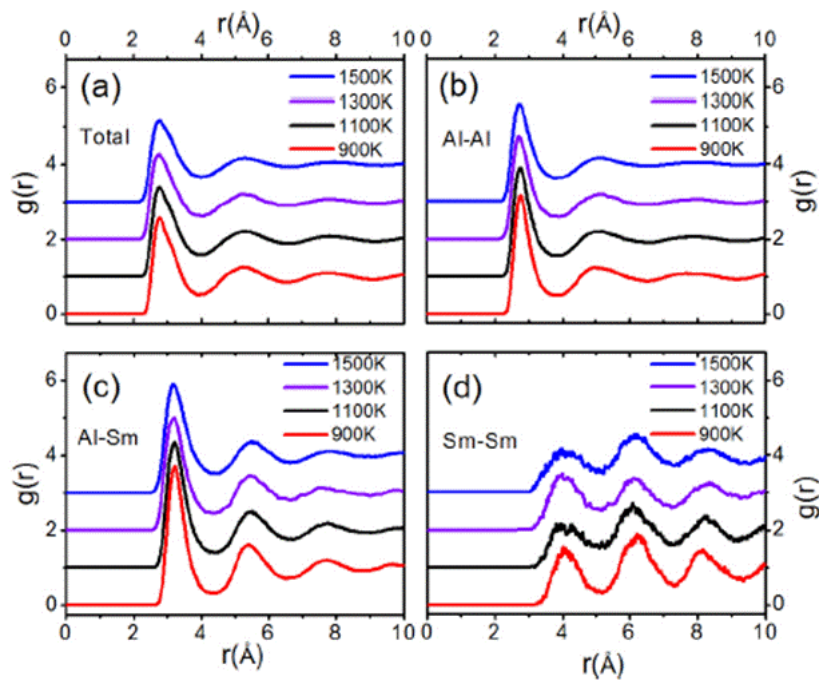
Figure 2.3. (a) Total, (b) Al-Al partial, (c) Al-Sm partial and (d) Sm-Sm partial PCF patterns of $Al_{90}Sm_{10}$ alloy at different liquid temperatures. Adopted from [47].
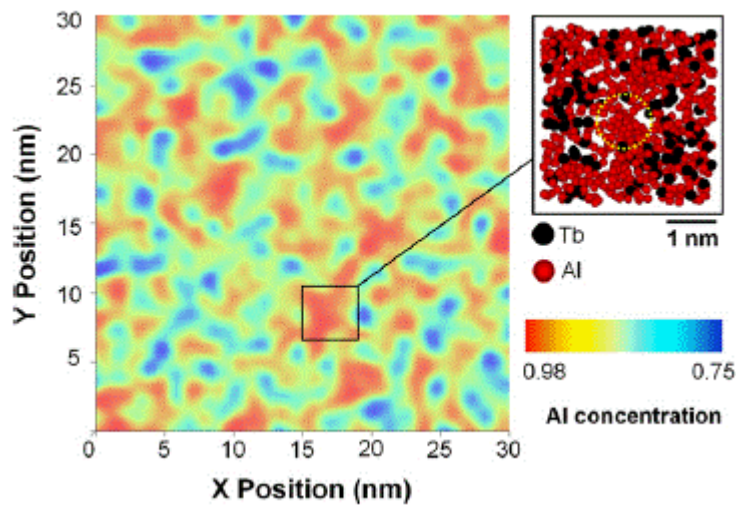
Figure 2.4. 2-D Al concentration map of amorphous $Al_{90}Tb_{10}$ alloy with 3-D APT results of 4 x 4 x 4 nm scaled volume inset that shows pure Al clusters. Adopted from [26].

The RMC simulations were used to construct the 3-D configurations to investigate higher order correlation in the medium range order scale. In order to emphasize the consistency of RMC, the simulations were supported by ab-initio MD results. The chemical and topological

orders in the simulated cells were investigated in details with Voronoi polyhedral and Warren-Cowley cluster analyses.

2.3. Experimental Procedure

2.3.1 Alloy Production

The $Al_{91}Tb_9$ ingots were produced by electric arc melting under Ar atmosphere. The ingots have been produced by highly pure Al (99.99 wt%) and Tb (99.9 wt%) elements. Amorphous ribbons with a width of 2.0-3.0 mm and a thickness of 30-50 μm were produced from bulk alloy by Cu block single melt spinner under Ar atmosphere at a tangential speed of 30 m/s. The samples were prepared in Ames Laboratory, USA [49]. The final compositions were verified by using microprobe analysis. The produced $Al_{91}Tb_9$ ribbons are shown in Figure 2.5.
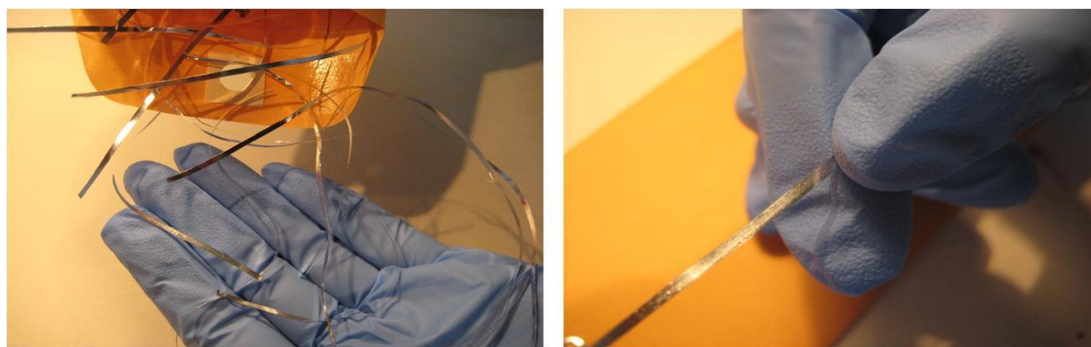
Figure 2.5. Melt-spun $Al_{91}Tb_9$ alloy ribbons.

2.3.2 High Energy X-ray Diffraction Analysis

The high energy X-ray diffraction studies were held by using the high-energy transmission synchrotron X-ray diffraction (HEXRD) at the Advanced Photon Source at Argonne National Laboratory in collaboration with the Midwest Universities Collaborative Access Team (MUCAT). Initially, the samples were cast into rods, then pieces of the rod were inserted into 2 mm diameter, carbon-lined quartz capillaries and sealed in Ar. The sealed carbon-lined quartz capillaries were heated up to 1323 K and exposed to 100 keV of X-rays corresponding to a wavelength of 0.0124 nm. The diffraction data were collected in transmission (Debye-Scherrer) geometry by a MAR charge coupled device (CCD), with up to 60 s of exposure time. During the experiment, no reaction between the liquid melt and the carbon-lined quartz capillary has been observed. A diffraction pattern from a similar carbon-lined empty quartz capillary was collected and subtracted from the liquid data sets for the background corrections. The diffraction data from the solid amorphous samples were collected without using any sample holder at room temperature.

Correction of raw HEXRD data has been performed for the background. The data have been converted to the total structure factor function, S(Q), according to the equation,

$$S(Q) = 1 + \frac{I^c(Q) - \sum_{i=1}^{n} a_i |f_i(Q)|^2}{\left| \sum_{i=1}^{n} a_i f_i(Q) \right|^2}$$

Equation 2.1

where $I^c(Q)$ is the coherent scattering intensity normalized to the atomic concentrations, a, and f(Q) is the atomic structure factors for each component in the system as corrected for polarization, absorption, multiple and Compton scattering [33].

2.3.3 Simulation Analysis

In order to build-up efficient 3-D illustrations, the structural models of amorphous structures were constructed by using ab-initio and RMC simulation techniques. The ab-initio Molecular Dynamics (MD) simulations were performed by using Vienna Ab-initio Simulation Package (VASP). The projector augmented wave (PAW) method is used for the description of electron – ion interactions. Periodic boundary conditions were applied with constant number of particles, volume and temperature (NVT) by using Nosé-Hoover thermostat to control the temperature [28-31]. In order to estimate initial number densities for $Al_{91}Tb_9$, the linear combination of pure Al and Tb elements were used. The exchange – correlation function has been described with generalized gradient approximation (GGA) of Perdew – Burke – Erhzernhof formulations. In a box cell, 200 atoms were distributed randomly with correct stoichiometry of the alloys. Initially, system was heated up to 2500 K to erase the memory effects for preparing the liquid Al-Tb alloy then subsequently cooled down to. 1900 K, 1700 K, 1309 K, 1247 K, 1208 K and to room temperature (300 K) respectively.

RMC simulations were held by using RMC++ simulation package [32] in order to construct 3-D configuration with large number of atoms. This provided studying the longer range correlations within amorphous and liquid states. 20,000 atoms with the proper stoichiometry, density and nearest neighbor distances were distributed randomly in a cubic box with periodic boundary conditions. Simulations were constrained with experimentally measured S(Q) and ab-initio MD simulated partial pair-correlation function to overcome the fundamental weaknesses of RMC [11, 32]. In describing the short range topological and chemical order in amorphous and liquid structures, the effectiveness of ab-initio MD is widely accepted. Therefore, the density of the alloy and the first shell neighborhood of Al and Tb atoms were constrained under MD simulations. For the first shell neighborhood determination in RMC analysis, the cut-off distances for the partial pairs were chosen from direct Fourier transforms of experimental S(Q) and ab-initio MD calculations. The difference between the measured S(Q) from HEXRD experiments and the calculated $S^C(Q)$ from each RMC modeled configuration is determined by

$$\chi_0^2 = \sum_{i=1}^{n} \frac{[S_0(Q_i) - S_0^c(Q_i)]^2}{\sigma(Q_i)^2}$$

Equation 2.2

In order to minimize the χ^2, approximately 10^6 iterations were performed for a constant $\sigma(Q)$ value of 0.002.

As mentioned before, the Voronoi Tessellation was used to define the local atomic configuration [33]. All polyhedrons were constructed in 5-digit Voronoi indices in as <N_3 N_4 N_5 N_6 N_7> where each digit represents N_i number of i-edged faces. Voronoi indices were also used to determine the nearest neighbors. Warren-Cowley parameter (α_{Al-Tb}) was used to investigate local chemical environment [35-36] by using the formula in Appendix 2.

In order to expand the range of chemical investigation, the second nearest neighbor atoms were taken into consideration by using a modified version of the parameter (α'_{Al-Tb}).

2.3.4 X-ray Diffraction and Transmission Electron Microscopy Analysis

The conventional XRD analyses were held by Cu-K$_\alpha$ between 5-95 2-theta degrees at a rate of 0.2 degrees/min from both sides of ribbon samples. TEM analyses were conducted by a JEOL JEM2100F scanning/transmission electron microscope. Samples for electron microscopy were prepared in four steps. First step was to obtain the proper dimensions by preparing coupons with 3 mm diameter and less than 50 nm thickness. In second step, the dimpling of the center of each coupon with Fischione Model 200 Dimpling Grinder was performed. The third step was the perforation of the samples via a Fischione Model 110 Twin Jet Electropolisher at 235 K with a solution of 25 vol% HNO$_3$, 75 vol% methanol. Last step consists of plasma cleaning of specimens for TEM analyses. This step was conducted with Fischione (Model 1020) Plasma Cleaner for 1 minute. The figures of specimen preparation instruments are shown in Figure 2.6.
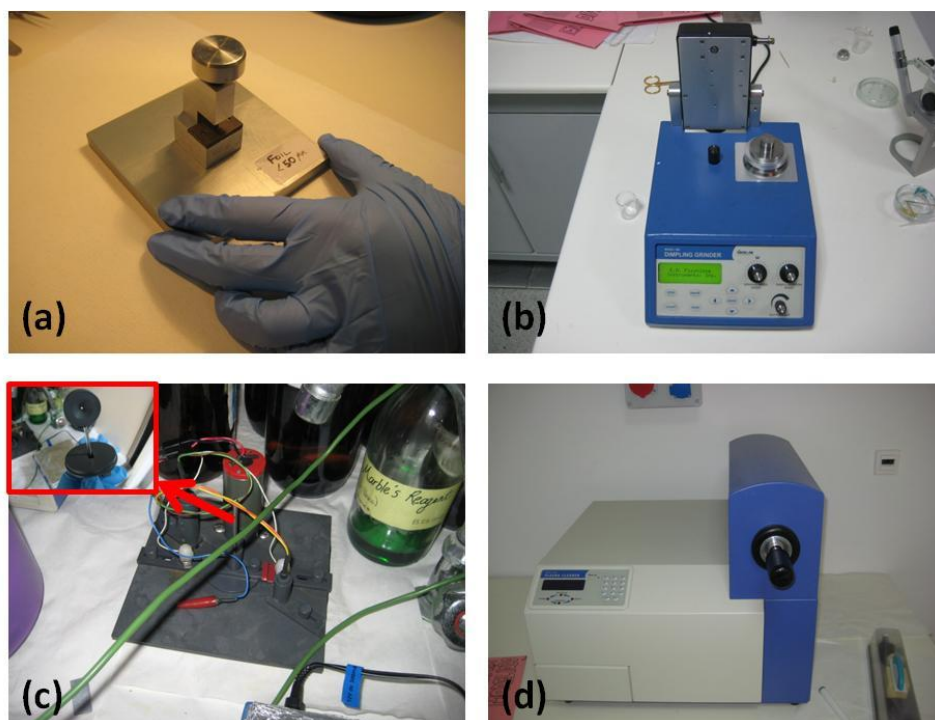
Figure 2.6. Figures of specimen preparation instruments (a) punch, (b) dimpler, (c) electropolisher (lollipop inserted) and (d) plasma cleaner.

2.4. Results and Discussion

The as-quenched $Al_{91}Tb_9$ specimens were initially investigated by TEM. The bright field (BF) image and representative selected area diffraction pattern (SAED) revealed a fully amorphous structure as shown in Figure 2.7(a). Both BF and the high resolution TEM (HRTEM) analyses showed no crystal structure within their limitations. The SAED and the fast-Fourier transformation (FFT) of the real-space image (insets) show a clear diffuse scattering. An interesting observation was the light contrast at relatively low reciprocal space in FFT pattern (Figure 2.7(b)- inset). This halo was referred to a pre-peak formation in reciprocal space.

As shown in Figure 2.8(a) and (b), the high-energy and conventional Cu K_α XRD analyses resulted in the same pre-peak formation at almost exactly the same position with FFT of HRTEM. Besides the pre-peak; in XRD pattern, a broad side-peak at a position of 34 nm^{-1} was also detected for amorphous specimen. As it was stated before, the HEXRD (X-ray diffraction with transmission geometry), Cu $K\alpha$ (X-ray diffraction with reflection geometry) and HRTEM (electron diffraction) experiments were collected from free standing specimens. According to this, the pre-peak which was revealed by three independent techniques, should be resulted from the structural features rather than any effects of specimen holders. Relatively faint pre-peak formation was also observed in the liquid state at 1208 and 1309 K as shown in Figure 2.8(a).

In order to determine the positions of main amorphous and extra reflections, a Lorentzian function was fitted to the HEXRD curves. Although the complete structure is amorphous, an expression [33] given as

$$R \approx 2\pi/Q_{\text{pre-peak}} \hspace{4cm} \text{Equation 2.3}$$

commonly used to represent the structural unit size. This expression presents a pseudo repeating unit with respect to the interplanar spacing in conventional crystals in some sense.
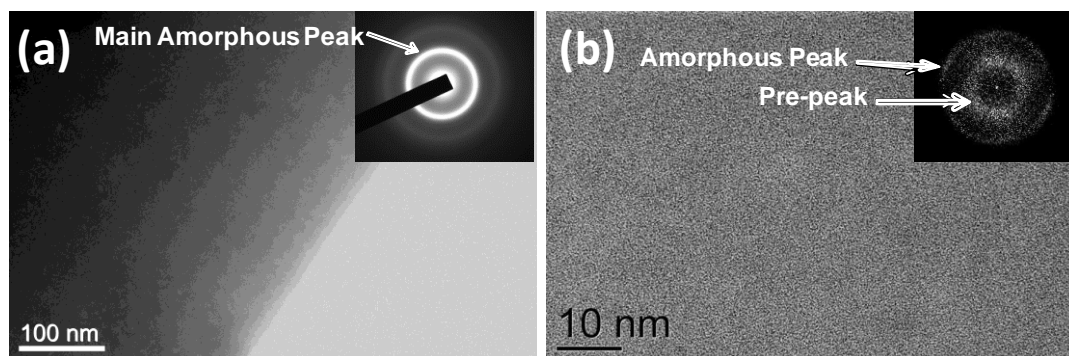
Figure 2.7. (a) BF images with SAED (inset) showing amorphous matrix for $Al_{91}Tb_9$, (b) HRTEM image with FFT (inset) showing the amorphous peak and pre-peak.
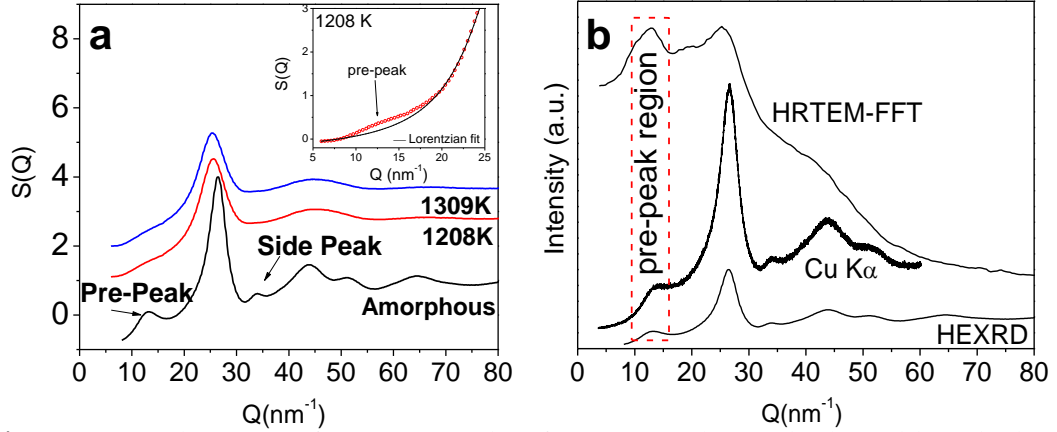
Figure 2.8. Total structure function S(Q) data for (a) amorphous $Al_{91}Tb_9$ and liquid $Al_{90}Tb_{10}$ alloy at 1208K, and 1309K with a given offset. Pre-peak at 1208K (inset) is indicated. (b) S(Q) data for amorphous alloy with XRD pattern and FFT of HRTEM (defocus: 15nm) showing the pre-peak.

Another expression similar to Scherrer equation used for determination of grain size in crystals was used to point out the proportions of any higher order structure represented by extra reflections in XRD [33]. This expression was given as

$$D \approx 2\pi/\Delta Q_{pre\text{-}peak} \qquad\qquad\qquad\qquad \text{Equation 2.4}$$

where D is the correlation length and ΔQ is the half-width of the pre-peak on the S(Q)-Q pattern. The results of these measurements and calculations are presented in Table 2.1.

Table 2.1. Positions of the pre- and the main amorphous peaks, the structural unit size and correlation length for amorphous and liquid alloys.

Alloy	Pre-peak (nm-1)	Structural unit size (nm)	Correlation length (nm)	Side peak (nm-1)	Main amorphous peak (nm-1)
Amorphous	12.9	0.486	2.4	34	26.5
Liquid 1208 K	12.6	0.495	1.1	*	25.6
Liquid 1309 K	*	*	*	*	25.4

* Poor Lorentzian fit because of the background.

As it can be observed in Figure 2.9, the partial pair correlation function (PCF) was calculated by ab-initio MD simulation using 182 Al and 18 Tb atoms within a cubic unit cell at 1309, 1208 and 300 K temperatures. It is significant that the height of the first peak increases with

decreasing the temperature. The positions on the other hand, move to higher distance with cooling down the system to lower temperatures.
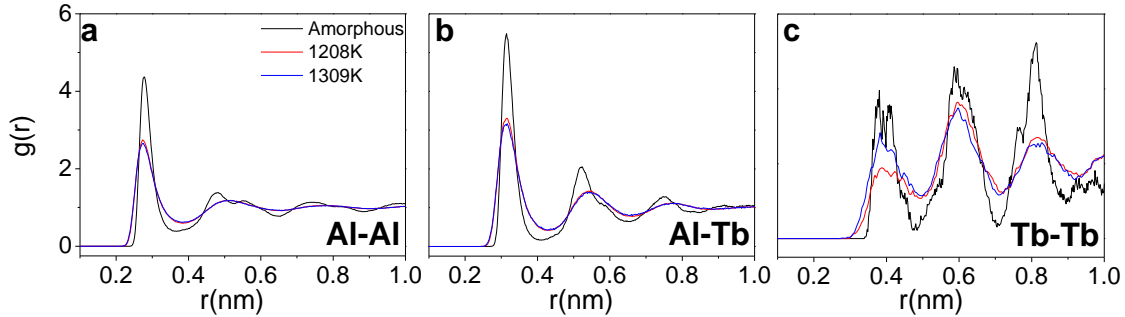
Figure 2.9. Partial pair distribution functions (PDFs) for amorphous and three different liquids of Al$_{91}$Tb$_9$ alloy for (a) Al-Al, (b) Al-Tb and (c) Tb-Tb respectively.

The lack of sampling caused, Tb-Tb correlations to be noisier as compared to Al-Tb and Al-Al PCFs. One interesting observation was the increase in Tb-Tb PCF intensity in the second and third shells. Ab-initio is an effective technique to study the topological and chemical correlations at short-range order (SRO). However its slow-moving dynamic nature results in chaotic outcomes when extending its capabilities beyond the first nearest-neighbor shell. In that manner, RMC calculations were conducted using 20,000 atoms via experimentally collected synchrotron HEXRD S(Q)-Q data as the input data. In order to overcome the well-known entropy problems of RMC [11, 32], the density, cut-off distances and first shell neighborhood (SRO) were constrained with ab-initio MD calculations. The cubic unit cell used in RMC corresponds to approximately 7.8 nm in length which is well designed to study medium and longer range correlations. The measured and calculated structure factors S(Q), are both shown in Figure 2.10. At liquidus and the amorphous temperatures, a significantly good matching of the experimental data and the simulation results including the pre-peak region.

The PCFs of amorphous and two different liquids of Al$_{91}$Tb$_9$ alloy were also calculated using RMC analysis and the results have been compared with ab-inito analysis. A remarkably good fit was also observed for PDFs in Al$_{91}$Tb$_9$ alloys especially in Al-Al and Al-Tb curves. The fitting of different PDFs can be observed in Figure 2.11.

The partial structure factor functions were calculated by RMC analysis. The results for Al-Al, Al-Tb, and Tb-Tb pairs respectively are indicated in Figure 2.12. From this figure it is obviously seen that partial structure factor for Tb-Tb pairs is much stronger than the ones in Al-Al and Al-Tb pairs in both pre-peak and side peak regions. This should greatly affect the existence of these extra broad peaks in the total structure factor function.
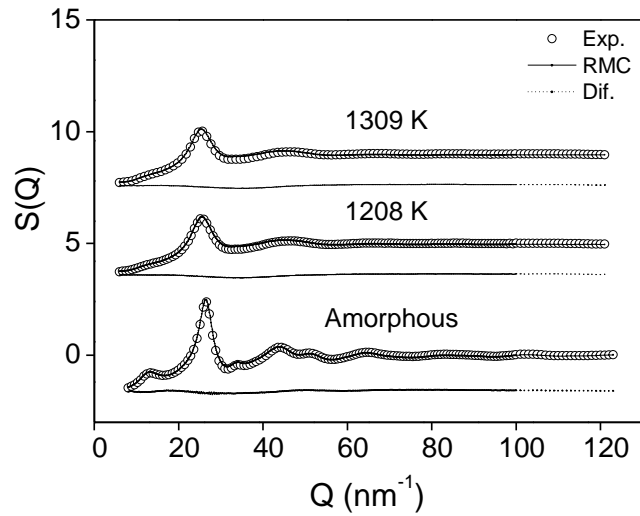
Figure 2.10. Total structure function data measured (circles) and calculated using RMC (solid line) for amorphous and two different liquids (at 1208 K and 1309 K) Al$_{91}$Tb$_9$. The dotted lines show the difference between experimental and calculated S(Q) data.

In order to seek the existence of any longer range correlations; 3-D configuration created by RMC was further investigated with several polyhedral analyses. Figure 2.13 highlights the predominant types Voronoi polyhedra (VP) in amorphous and liquid configurations.
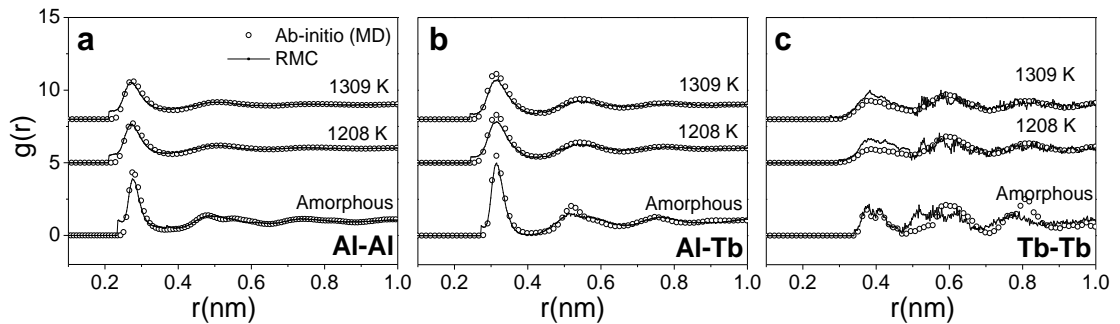
Figure 2.11. Partial pair distribution function (PDFs) data calculated using ab-initio (circles) and RMC (solid line) for amorphous and two different liquids of Al$_{91}$Tb$_9$ alloy for (a) Al-Al, (b) Al-Tb and (c) Tb-Tb respectively.

These indices were constructed according to the center atom type. For Al centered polyhedras the most favored cluster is <0,3,6,4,0> in all temperatures. The other common type of VP are as follow; <0,2,8,4,0>, <0,1,10,2,0> for amorphous, <0,2,8,2,0>, <1,3,4,5,1> for 1208 K and <1,3,4,5,1>, <0,3,6,3,0> for 1309 K. When compared to Al atoms, the Tb atoms are much more coordinated. The most preferred VPs are; <0,2,8,6,0>, <0,1,10,4,0>, <0,1,10,5,0> for amorphous, <0,2,8,5,0>, <0,3,7,5,1>, <0,3,6,6,0> for 1208 K and <0,3,7,5,1>, <0,2,8,5,0>, <0,3,7,4,1> for 1309 K. Although the perfect icosahedral structure with a VP index of

<0,0,12,0,0> is not on the top list several icosahedral like VPs like <0,2,8,2,0>, <0,1,10,2,0>, <0,3,6,4,0> were detected particularly around Al atoms.
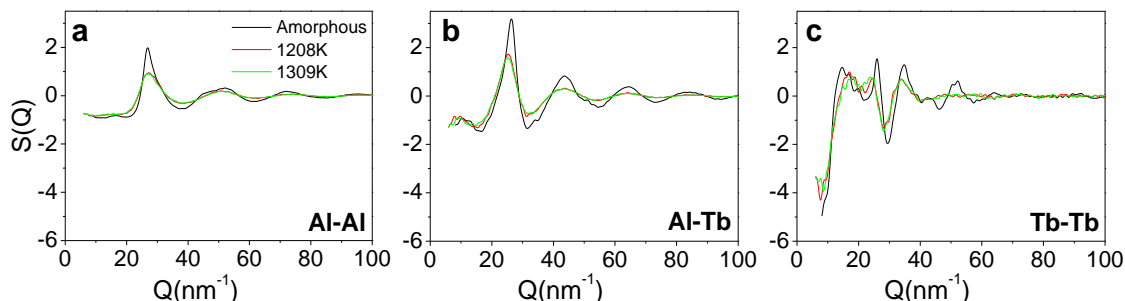
Figure 2.12. Partial structure factors S(Q) calculated for amorphous and two different liquids (1208K and 1309K) for (a) Al-Al, (b) Al-Tb and (c) Tb-Tb respectively.

In contradiction to Al atoms, Tb atoms prefer to host bcc-like clusters such as <0,2,8,6,0>, <0,1,10,5,0> and <0,2,8,5,0>. Within the context of Voronoi Tessellation analysis, each atom in the space can be represented by a Voronoi polyhedron such that number of faces forming a polyhedron corresponds to the coordination number of the given atom. Every single face of the polyhedron determines the border between the central atom and one of its neighboring atoms, and the number of edges forming the face gives the number of common neighbors of the corresponding atom pair. According to that, the method provides strong information about local atomic distribution of the system in different conditions. From higher liquidus temperatures to quenched amorphous phase, the diversity of Voronoi indices were decreased from 2746 to 1475 species (300K**:**1123 Al-centered, 352 Tb centered, 1208K**:** 1934 Al-centered, 663 Tb-centered, 1309K**:** 2038 Al-centered, 708 Tb-centered) underlying an increase in order. In addition, particular dominant types of polyhedrons have been noticed as seen in Figure 2.13. According to the classification made before [50], among Al-centered clusters, in glass state the icosahedral-like group such as <0, 0, 12, 0, 0>, <0, 1, 10, 2, 0> and <0, 2, 8, x, 0> (with low x values) were highly increased. Existence of crystal-like groups (e.g. <0, 4, 4, x, 0> where x=4, 5, 6) is also a bit more developed in glass while still present in liquid. It is also obviously seen that an increase in icosahedral-like Tb-centered clusters in liquid state happens. The complete short-range topological evolution strongly reminds the one in previous study on Al-Sm marginal glass former system [22].

These polyhedra analyses are sensitive to small angular distortion which results in a relatively large number of varieties of clusters. On the other hand, while considering the coordination number (CN) calculated from VP analysis, it is obvious that the distribution is much narrow. In Figure 2.14, the histograms indicate the CN around Al and Tb atoms for all amorphous and liquid states. The average CN around Al and Tb are also shown in Table 2.2. Relatively higher CN was detected for Tb center clusters in first shell neighborhood.

The bond angle fractions between four different atomic triplets were calculated and shown in Figure 2.15. According to these distributions, the maximum and minimums of the angular

fractions nearly remains the same in two different liquid temperature and the amorphous states.
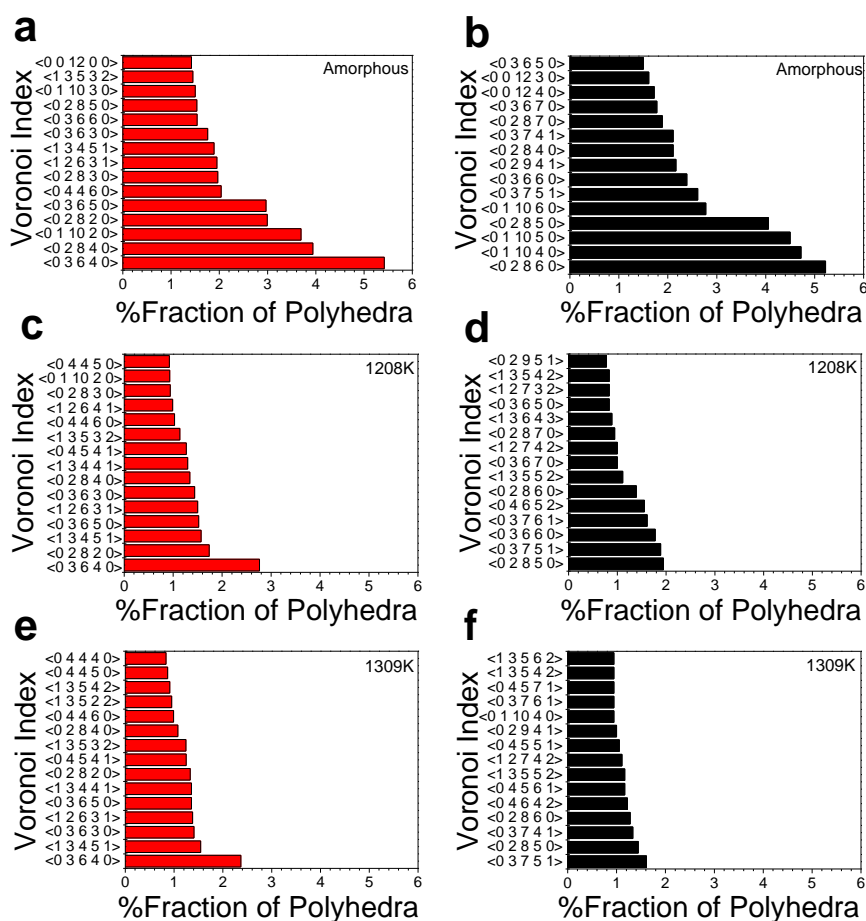
Figure 2.13. Most populated VP histograms of (a, c, e) Al and (b, d, f) Tb centered structure models for amorphous (a, b), 1208K (c, d) and 1309K (e, f) $Al_{91}Tb_9$ alloy.
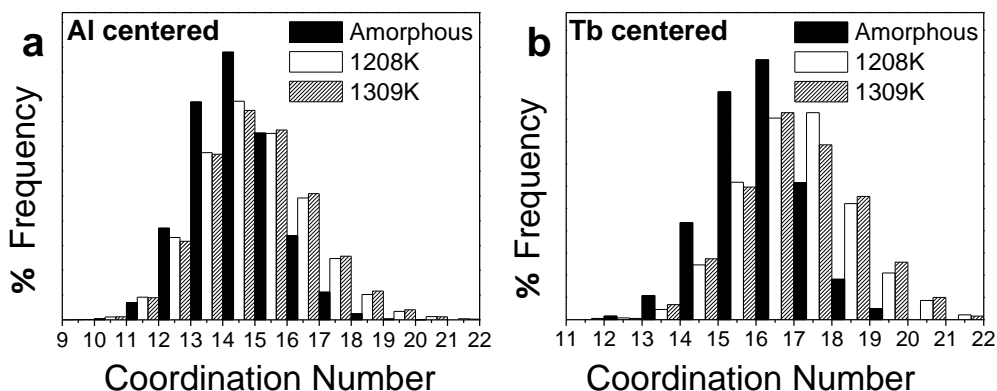
Figure 2.14. Coordination numbers calculated for (a) Al and (b) Tb centered VP models for amorphous and two different liquids (1208K and 1309K) of $Al_{91}Tb_9$ alloy.

Table 2.2. Average coordination numbers (CN) around Al and Tb for amorphous and liquidus temperatures respectively.

Temperature	Average CN Around Al	Average CN Around Tb
Amorphous	14.0	15.8
Liquid 1208 K	14.2	16.2
Liquid 1309 K	14.3	16.1

When the triplets in Al-Al-Al and Al-Tb-Al reveals very close angular distribution, the values shift through higher angles in Tb-Al-Tb and Tb-Tb-Tb triplets. In addition, a considerable reduction in the differences of percent fractions between amorphous and the liquid states is observed in Figure 2.15(c) and (d).
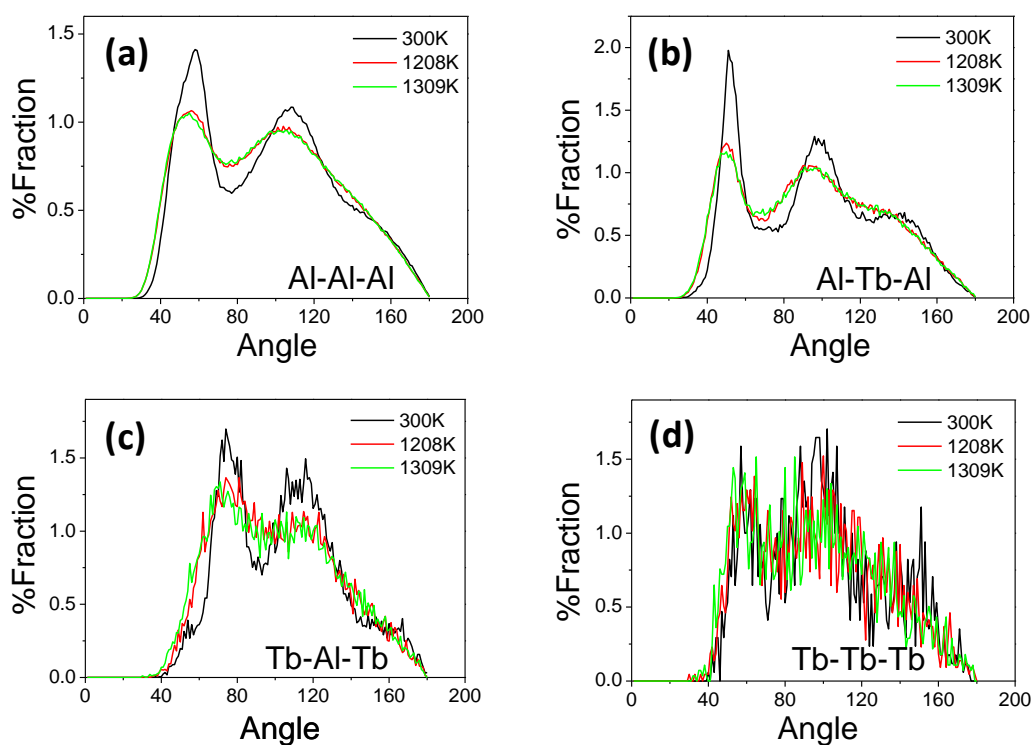
Figure 2.15. Bond angle distribution in amorphous (300K) and liquid (1208K and 1309K) of (a) Al-Al-Al, (b) Al-Tb-Al, (c) Tb-Al-Tb and (d) Tb-Tb-Tb atom triplets.

As it was stated before, the pre-peak observed on amorphous diffraction patterns collected by X-ray or neutron diffraction, also called as first sharp diffraction peak [51], has been discussed extensively in the literature. The structural origin of the pre-peak has often related to quasi-periodic crystal [51], chemical short-range order [11], structural medium-range order (MRO) [52], and ordered interstitial void formation [51] within the disordered structure. In the previous studies with $Al_{90}Sm_{10}$ marginal glass forming alloys some MRO structure corresponding to a high-temperature metastable pseudo-tetragonal $Al_{11}Sm_3$ (SG:I4/mmm) were detected by HEXRD and RMC studies [33]. Similarly, FEM analyses indicated MRO of pseudo-trigonal Al_3Tb that underlined for as-quenched $Al_{90}Tb_{10}$ alloy [26]. The HEXRD and ab-initio constrained RMC results reveals the existence of common structural correlations with the tetragonal $Al_{11}Tb_3$ (SG:I4/mmm) and metastable hexagonal $Al_{17}Tb_2$ (SG:P63/mmc). Although a tetragonal $Al_{11}Tb_3$ (SG:I4/mmm) structure has not been yet reported for Al-Tb system, it should be noted that Al-Tb is not a well-studied binary alloy system. In this study, a hypothetical t-$Al_{11}Tb_3$ with I4/mmm space group symmetry is adapted by correcting the lattice parameters using corresponding atomic radii. Schematic views of hypothetical tetragonal $Al_{11}Tb_3$ and metastable hexagonal $Al_{17}Tb_2$ is given in Figure 2.16.

(a)

0.45 nm

20 Al atoms around Tb
<0.36 nm

18 Al atoms around Tb
<0.36 nm

(b)

0.42 nm

16 Al atoms around Tb
<0.32 nm
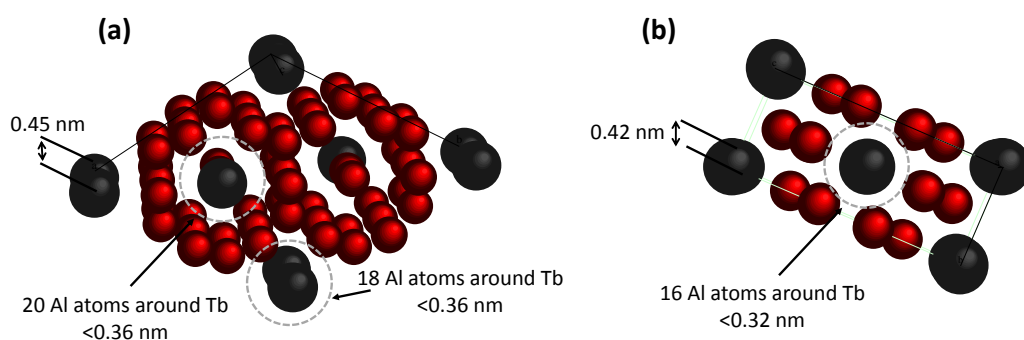
Figure 2.16. 3D representation of (a) h-$Al_{17}Tb_2$ (SG:P63/mmc) and (b) hypothetical t-$Al_{11}Tb_3$ (SG:I4/mmm) compounds. The lattice parameters for hypothetical t-$Al_{11}Tb_3$ were estimated using atomic radii.

All of these structures have strong Bragg reflections around 12.8 nm^{-1} which matches with the observed position of the pre-peak in amorphous Al-Tb system [26]. The atomic configurations calculated by ab-initio constrained RMC simulations have also similarities with these two intermetallic structures.

It should be noted that the main scope in this analysis is not to fit the extra peaks in HEXRD pattern but to pay attention to the specific distribution of the atoms within these crystal structures which give rise to high coordination of RE atoms and Bragg reflections at pre-peak position. When these crystal structures are considered, it is clearly seen that they consists of repetition of SRO clusters of Tb centered atoms surrounded by a definite number of Al atoms. Particularly, in h-$Al_{17}Tb_2$ and t-$Al_{11}Sm_3$ clusters of Tb with 18 or 20 Al atoms and

16 Al atoms are self-repeating, respectively. The repetition of Al surrounded Tb clusters naturally causes the high-coordination number around RE atoms, and gives specific Al-Al, Al-RE and RE-RE distances in the first shell neighborhood. According to this determinations, correlation to MRO clusters of Tb centered Al atoms is more meaningful than directly relating the disordered structure to well-defined crystal structures of Al-Tb. The correlation length calculated from HEXRD is on the order of 2.4 nm for the solid amorphous state which corresponds to 5 or 6 repeating layers of corresponding planes for pseudo crystal structure.

In that manner, the Tb centered Al atomic clusters are thought to exist in the as-quenched state by forming a network of MRO structure. The formation of a network was previously shown by atom probe tomography experiments in Al-Tb amorphous system [26]. The results of this previous study indicated regions of interconnected Tb rich network separating pure Al islands with an average size of 1 nm. The results of current and previous study [26] obviously present chemical separations of Al and Tb rich regions. In order to reveal the reason for such a chemical separation in amorphous state, the structure of liquid Al-Tb should be considered. According HEXRD constrained with ab-initio, it is hypothesized that some Tb centered clusters of Al atoms exist in the amorphous state which give rise of the pre-peak at low scattering angles. In addition, the same pre-peak also present for the liquid state that points out the existing of the same clustering effect in the molten state at elevated temperatures. This results regions of Al and Tb rich clusters in liquid as well. Therefore, in terms of the atomic distribution, the as-quenched liquid is not as homogeneous as it is expected. In order to represent this inhomogeneity, Warren-Cowley parameter was calculated for Al atoms in glass and liquid states and its fractional distribution is given in Figure 2.17(a). In order to investigate longer chemical correlations "expanded" Warren-Cowley parameter was also calculated by including second-nearest neighbor shell surrounding Al atoms as shown in Figure 2.17(b). Aluminum atoms having "expanded" Warren-Cowley parameter equal to unity and their surrounding atoms up to second-shell (all are aluminum) were plotted in Figure 2.18 in order to visualize pure-aluminum domains both in liquid and glass.
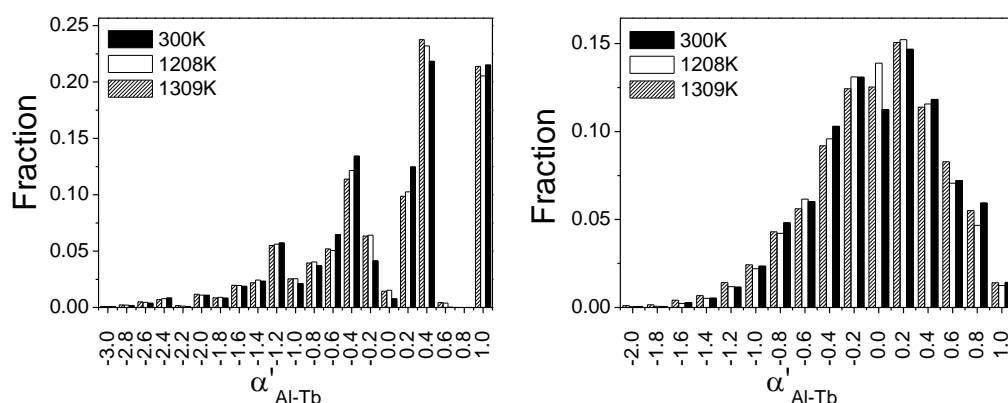
Figure 2.17. Classical (a) and "expanded" (b) Warren-Cowley parameter distribution of Al atoms in amorphous (300 K) and liquidus (1208 K and 1309 K) states.

The chemical fluctuations were determined in SRO both in liquidus and amorphous states during Warren-Cowley analysis. The parameter of Al atoms (α_{Al-Tb}) are widely distributed that shows the signs of fluctuations. In order to investigate whether these fluctuations are present in medium range scale, "expanded" Warren-Cowley parameter (α'_{Al-Tb}) were calculated as mentioned and by introducing the next nearest neighbors surrounding Al atoms, an evidence of medium range chemical ordering, were observed corresponding to pure aluminum domains of dimensions higher than 1 nm covered by Tb-rich network. The illustration can be seen in Figure 2.18.
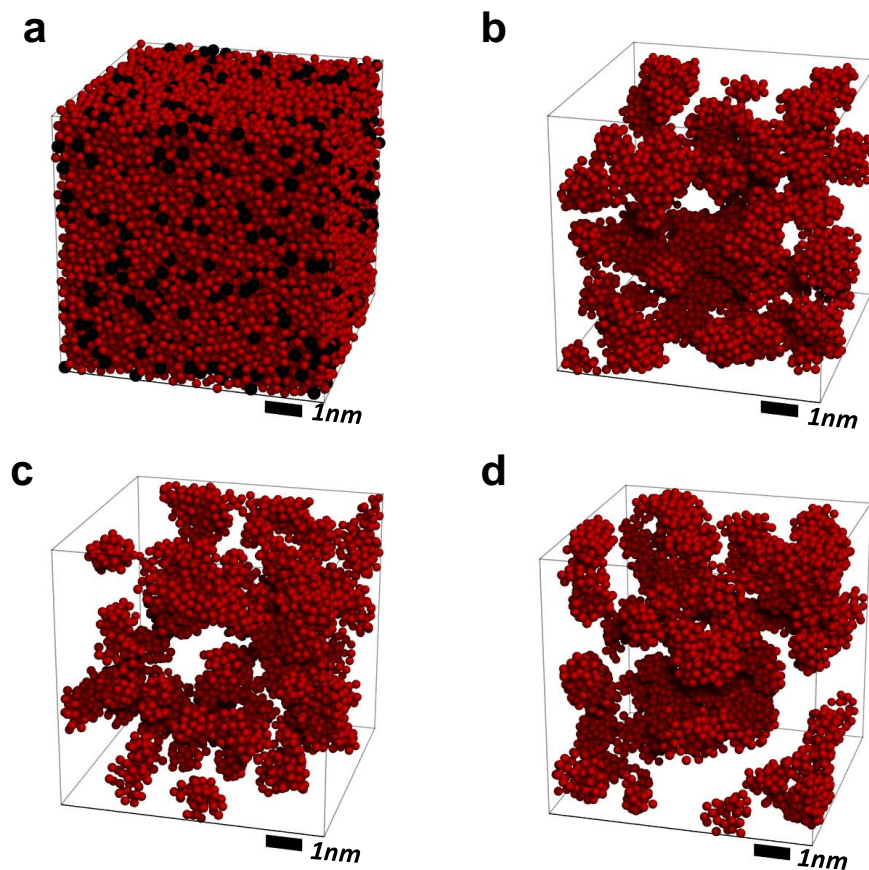
Figure 2.18. Three dimensional atomic configuration of (a) amorphous (300 K) from RMC and pure-aluminum domains in (b) 300 K, (c) 1208 K and (d) 1309 K.

According to the previous APT and current ab-initio constrained HEXRD results, it is believed that Tb atoms (this can be also attributed to other RE) within the liquid structures are highly correlated with Al atoms which results in chemical separation of Tb and Al rich regions. Each region may possess MRO structure having some pseudo-crystal periodicity. Upon rapid solidification, Tb-rich clusters dividing the matrix into nanoscopic regions prevent the crystallization of the molten metal. The as-solidified structure has similar chemical separation with larger correlation lengths as calculated from HEXRD. The findings

on pure aluminum domains obtained from structural and chemical analysis on RMC simulations based on X-ray scattering experiments are congruent with the recent similar results in Al-Tb system with similar composition in glassy state by atom probe tomography [26] and projects the structural origins of these domains in liquid at temperatures higher than the melting temperature. It is believed that these domains are gathered into larger regions during structural relaxation at low-temperature annealing, and become responsible of two main results that are the potential nucleation sites for fcc-Al nanocrystals and the rare earth-concentrated network with high fraction of icosahedral-like groups enveloping these pure aluminum regions, acting as a diffusion barrier due to its low atomic mobility [53] and resulting the suspended growth of nanocrystals.

2.5. Conclusion

This chapter introduced the conditions for the local chemical and topological structures of amorphous Al-Tb before the controlled crystallization experiments. According to ab-initio MD and HEXRD constrained RMC results, the atomic configuration of as-quenched and liquid states are not fully disordered as it is expected from an amorphous and/or liquid structure. Some clear evidence of chemical and topological MRO was detected in $Al_{91}Tb_9$ as-quenched and molten states. The chemical and topological orders were identified by Warren-Cowley and Voronoi Tessellation methods respectively. Next chapter will discuss the devitrification mechanism for as-quenched Al-Tb alloy.

CHAPTER 3

NANOCRYSTALLIZATON KINETICS in Al$_{90}$Tb$_{10}$ ALLOY UPON ISOTHERMAL HEATING

3.1. Introduction

Devitrification products of marginal glass formers have recently got the significant attention due to the high number density of nanocrystal formation embedded in amorphous matrix. Despite the fact that this unique property of marginal glass forming alloy has already in practical used (i.e. FeNdB magnets), we're far from to come with a solid explanation for the unusual crystallization path. This following chapter tends to give insights of solid state crystallization mechanism giving rise to highly populated nanocrystals.

3.1.1 Nanocrystallization Pathways

When the practical production methods are considered, there are mainly four different types of nanocrystallization techniques [10]. First method is the several plastic deformations such as ball milling, equichannel angular pressing, and extensive rolling. It should be noted that extensive plastic deformation may cause some unwanted structural defects and chemical impurities. Second method is the chemical or physical vapor deposition technique. The main idea behind these methods is the condensation and deposition of the nanocrystalline materials on a substrate. Historically, this technique is assumed to be the first one to produce nanocrystalline metals [1-2]. Although it is quite effective, only a thin layer of nanocrystalline material can be produced by this technique. Therefore it is not suitable for mechanical applications. Third technique consists of rapid solidification. Under the proper solidification rates crystal can nucleate and restrictively grow because of the increased viscosity during cooling. Practically it is difficult to obtain a homogeneously distributed nanocrystal due to the variations in thermal gradient by applying this technique. The last method, which is also the subject of the current chapter, is the devitrification of an amorphous precursor material. Upon achieving an amorphous matrix, this method can be considered as the most convenient way of producing homogeneously distributed equal sized nanocrystals.

3.1.2 Theories on Devitrification Mechanism of Marginal Glass Formers

As it was stated before, the mechanism behind the high number of nanocrystal nucleation is still an enigma. Considering the Al-RE and Al-RE-TM amorphous alloys one of the first studies was performed by Perepezko and co-workers on Al-Sm and Al-Y-Fe systems. According their approach, considerable fraction of small crystalline nuclei formed during

rapid solidification. However, the rapid rising of viscosity near glass transition temperature (T_g) suppress the growth of these nuclei. Therefore, this crystallite, called as "quenched-in-nuclei" trapped within the amorphous matrix [23]. This hypothesis was tested by using melt-spun and cold-rolled Al-Sm amorphous specimen [23]. Although FEM showed fcc like MRO in melt spun specimens, signal was absent for cold rolled specimen. Instead a different type of order was detected. This was explained by the lack of quenched-in-nuclei formation in cold-rolled Al due to the fact that it was not produced by solidification. Furthermore they observed T_g for cold-rolled specimen but not in melt-spun ribbons which supports the existence of crystallite nuclei in the as-quenched state [46].

The second approach explains the nanocrystallization after an amorphous precursor under a mechanism similar to spinodal decomposition [42]. According to this second hypothesis, a fully amorphous state can be obtained upon quenching, however before crystallization a phase separation occurs in the matrix [41, 42]. The origin of the phase separation was explained through a time independent homogeneous nucleation theory called coupled-flux nucleation [42, 54]. According to this argument amorphous phase separates into Al-rich and Al-depleted zones prior to crystallization. Al-rich regions extend to 74-126 nm [41] are hold responsible for the nucleation of fcc-Al nanocrystals.

Both approaches were questioned on different aspects [21, 22, 26]. For instance, a phase separation was observed for $Al_{88}Gd_6La_2Ni_4$ [42] but a slightly different composition of $Al_{88}Gd_6ErNi_4$ does not show any indication of that [55]. Also, a two-stage fcc nanocrystallization was indicated for several Al-TM-RE amorphous alloys contradicting with "quenched-in-nuclei" hypothesis. The cold-rolling technique performed to show the suppressing of "quenched-in-nuclei" formation is also questionable on various aspects such as chemical integrity of the amorphous alloy [56].

A third approach relies on the fact that some nanoscale phase separation may actually present at nanoscales causing chemical and topological order to be formed up to some degree [21, 26, 27, 33, 41, 42, 54]. Kalay et al. have experimentally demonstrated regions of 1 nm pure Al in as-quenched $Al_{90}Tb_{10}$ [26]. The simulation results of this study (Chapter 2) are a good agreement with this experimental observation. The results of current and previous [33] work have also stated the possibility of having MRO structure in liquid state. This hypothesis should be tested further before giving a final conclusion.

As it was summarized, the enigmatic behavior of high number density nanocrystallization is unpuzzled. A common approach is to use well-known Johnson-Mehl-Avrami (JMA) principle [57-58]. Several JMA studies were conducted with Al-based metallic glass before such as Al-Y-Fe [59], Al-Ni-Y [60] and Al-Sm [33]. The results of such studies should be considered carefully. The reason for this is the possibility of having MRO or nanocrystal embedded in amorphous matrix which will disrupt the fundamental homogeneous amorphous matrix assumption by JMA [58]. Therefore the as-quenched structure should be investigated carefully before any JMA types of attempts.

This chapter will discuss the probability of JMA approach in marginal glass forming alloy systems.

3.2. Experimental Procedure

$Al_{90}Tb_{10}$ ribbons were produced as described in *section 2.3.1.*

3.2.1 Differential Scanning Calorimetry Analysis

Specimens for DSC were cut into equal size billets with 10 mg average weight. They were fed into Al pans and sealed with Al cover. Specimens were isochronally heated with 100^0C/min heating rate and isothermally hold at predetermined temperatures (220-214^{0}C) below crystallization point. After each run, same routine was repeated with empty pans to calculate the baseline.

3.2.2. Devitrification of Amorphous Alloy

Isothermally crystallized specimens for XRD, TEM, SEM and mechanical testing (Chapter 4) analyses were prepared using silicon oil bath. Specimens were kept in the bath at 220^0C for five predetermined time period. These periods were labeled as A, B, C, D, E as shown in Table 3.1. These labels represent different level of nanocrystallization during controlled devitrification experiments. The time required to reach 220^0C was measured by a thermocouple inserted in the bath and it was taken into consideration for JMA comparison. Oxidation levels of the specimens after the oil bath treatments were checked with energy dispersive spectrometry (EDS) analysis.

3.2.3. X-ray Diffraction and Transmission Electron Microscopy Analysis

The conventional XRD analyses (Cu-K$_\alpha$) were conducted at Bragg-Brentano geometry between 10-80 2θ degrees with a scan rate of 0.02 degrees/min. from both sides of ribbon specimens. TEM specimens were produced with the same procedure explained in *section 2.3.4.*

3.2.4. Number of Density Measurement

Number density measurements of nanocrystal at different levels of crystallization are crucial. In order to get significant calculations, 20 sets of data including 5 BF images of nanocrystals and 1 BF image of corresponding hole area were taken for each level. Therefore for each crystallization step considered in this study (A to E) 120 BF images were investigated with utmost care. Because of the resolution limitations, nanocrystals smaller than 5 nm were not considered. The volume number density is given by this following formula [61-62]

$$N_v = \frac{N_A}{t + \bar{d}} \qquad\qquad \text{Equation 3.1}$$

where N_v is volume particle density, t is the thickness, d is average particle size and N_A is the particle density per image. In this equation a key parameter is the thickness of the specimen. The thickness of specimen can be calculated by the well-known electron mean free path formula [63-64]

$$\frac{(I_{BF})}{(I_0)} = exp\left\{-\frac{t}{\Lambda}\right\} \qquad\qquad \text{Equation 3.2}$$

where I_{BF} is the bright field average intensity, I_0 is the bright field average intensity of fully transmitted beam (the hole), t is the thickness, and ⋏ is the elastic scattering mean free path. ⋏ is equal to 130 nm for Al [63]. An example of intensity measurement is shown in Figure 3.1

The average diameters of dendritic nanocrystals were estimated by measuring the distance between two edges of 10 crystals for each image. Therefore average sizes were estimated from 200 individual nanocrystal measurements for each set.
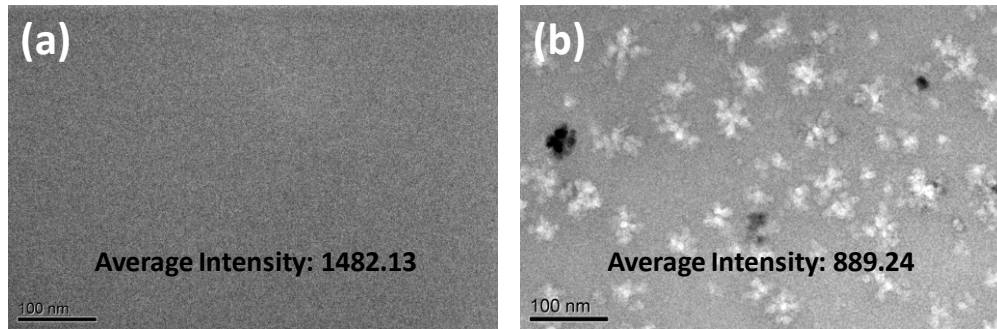
Figure 3.1. BF of (a) hole and (b) specimen with nanocrystals taken from state E with average intensities.

3.3. Results and Discussion

Figure 3.2(a) and (b) shows the DSC isothermal heating curves for 12 and 50 minutes respectively. The nanocrystallization of fcc completes by the first exothermic reaction in 22 minutes and then second reaction yielding to a Al-Tb intermetallic phase takes place. A representative BF image taken after the second exothermic reaction is shown in Figure 3.3. This figure shows the fcc nanocrystals, Al-Tb intermetallic phase and the remaining amorphous phase. The formation of this second phase is left out of scope of the thesis and the first reaction resulting in high number density of nanocrystal is taken under consideration. The annealing times shown in Figure 3.2 are given in Table 3.1
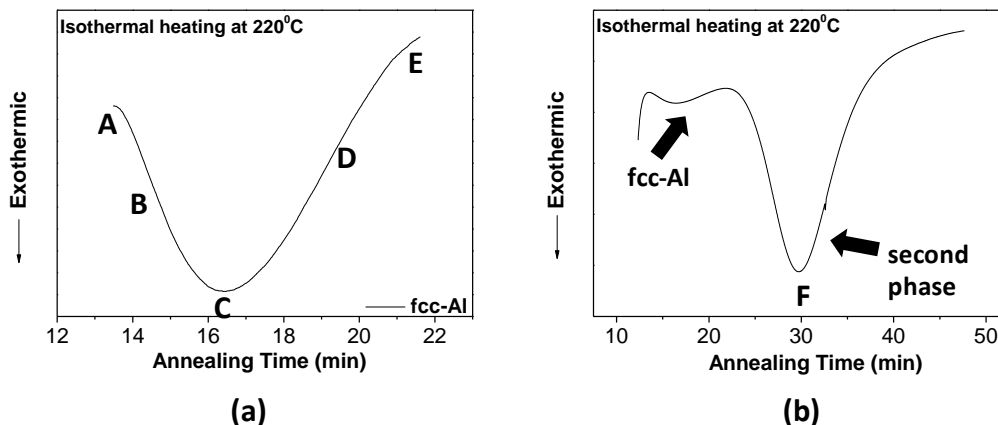
Figure 3.2. Isothermal DSC curves of (a) $Al_{90}Tb_{10}$ for fcc-Al part and (b) the overall reaction at 220^0C
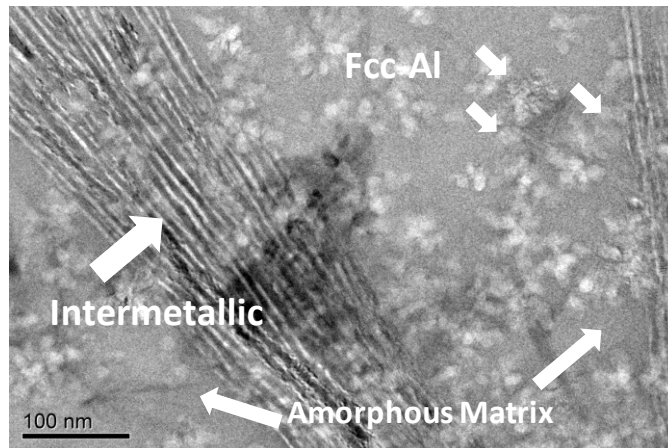
Figure 3.3. A representative BF image showing the fcc-Al and intermetallic phase with amorphous matrix.

Table 3.1 Annealing times of labeled states given in seconds.

Label	Time (seconds)
A	298
B	365
C	469
D	634
E	785
F	1270

Figure 3.4 shows the XRD patterns for A, C, E and F. In A the level of crystallization is so low that the fcc-Al peaks cannot be distinguished. Starting with C clear fcc-Al reflections are apparent. In F, reflections coming from the second phase (Al-Tb intremetallic) can be also seen in the XRD pattern. One intriguing observation is the transformation of the pre-peak into this second phase. It should be noted that second Al-Tb phase evolves from the remaining amorphous matrix. This detail definitely deserves further interest.

Figure 3.5 summarizes the first devitrification sequence captured by TEM. SAED patterns clearly indicate the evolution of the fcc-Al structure with respect to annealing time. Figure 3.6 and 3.7 shows the HRTEM taken for each condition. The amorphous nature of the precursors is seen in Figure 3.6 with no indication of any nanocrystalline structure. The FFT representing different zone axis of fcc-Al and Al-Tb intermetallics are seen in Figure 3.7(a) to (f). A clear and sharp boundary is present between the nanocrystal and the amorphous matrix.
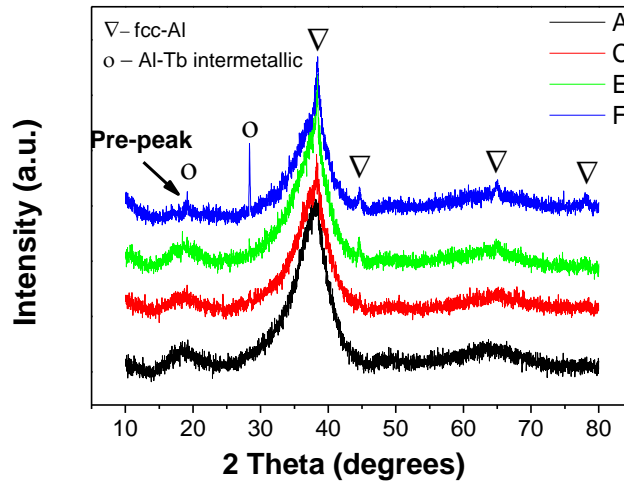
Figure 3.4. XRD patterns for A, C, E and F.

TEM investigations show an increase in average nanocrystal size with respect to annealing time. The average nanocrstalline size is on the order of 20 nm at A and almost linearly increase to 37 nm at point E (Figure 3.8(a)). An interesting observation was made on number density measurements. It seems that volume number density during annealing keeps constant. For all annealing condition this number stays around 2×10^{21} m^{-3}.

The devitrification kinetics was also investigated through JMA approach. The JMA equation [22, 58] is given as

$$x = 1 - exp\{-[k(t-\tau)]^n\} \hspace{3cm} \text{Equation 3.3}$$

where x is the volume fraction of the crystallized phase, t is the annealing time, n is the Avrami exponent, τ is incubation time and k is the rate constant. Among these parameters n is particularly important in transformation behavior determination. Christian summarized the possible nucleation and growth mechanisms with respect to different Avrami exponents (n) in [37].

Avrami exponent can be calculated from isothermal DSC holds. As it can be easily seen from Equation 3.3 the slope of ln(-ln(1-x)) versus ln(t-τ) gives the value of n. Figure 3.9 shows the percent fcc-Al nancrystallization versus annealing time excluding the incubation time (~ 1.2 sec.). It should be noted that although the fraction is up to 100%, there is considerable amount of remaining amorphous phase. This amorphous phase transforms to another Al-Tb intermetallic upon subsequent annealing. However, JMA is only meant to be applied to fcc-Al nanocrystallization. Therefore the 100% crystallized fraction represents the end of amorphous to fcc-Al phase transformation. At 220°C the overall nancrystallization process (excluding incubation period) takes 8 minutes. Figure 3.10 shows the JMA plot. For the approximate phase transformation range of $0.05 \leq x \leq 0.85$ the plot is almost linear.
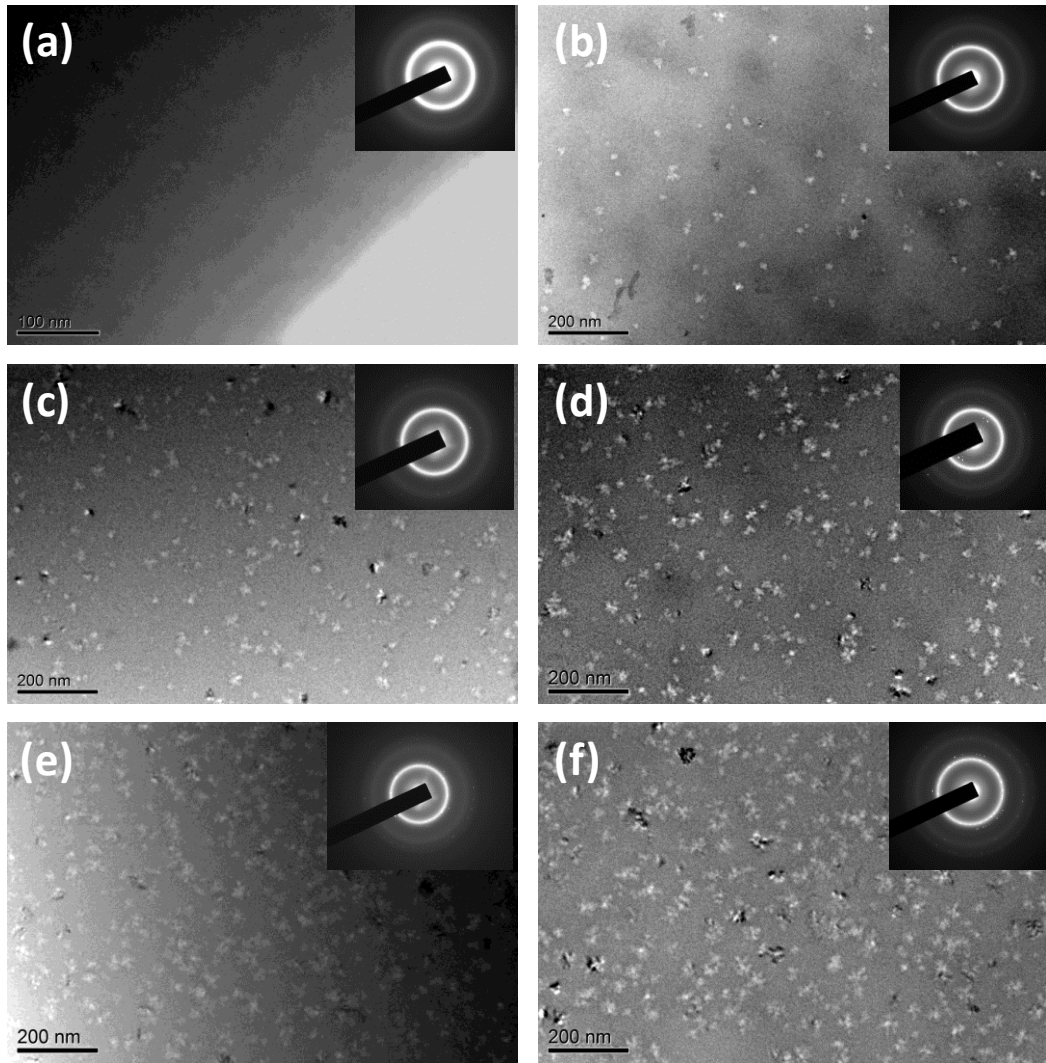
Figure 3.5. BF images of (a) amorphous, (b) A, (c) B, (d) C, (e) D and (f) E with SAED insets.
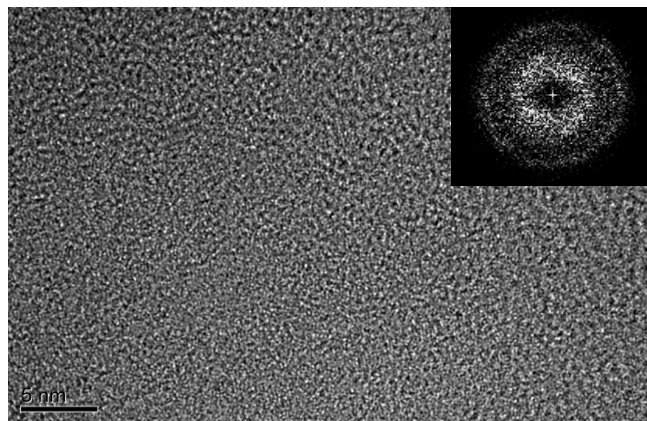
Figure 3.6. HRTEM image of amorphous phase with FFT inset.

The Avrami exponent (n) was calculated as 2.5. Such Avrami exponent represents a constant nucleation rate with diffusion controlled growth [37]. Another alternative way of conducting JMA analysis is to take the derivative of n with respect to crystallized fraction [65] given as

$$n(x) = \frac{\partial \ln(-\ln(1-x))}{\partial \ln(t-\tau)}$$

Equation 3.4
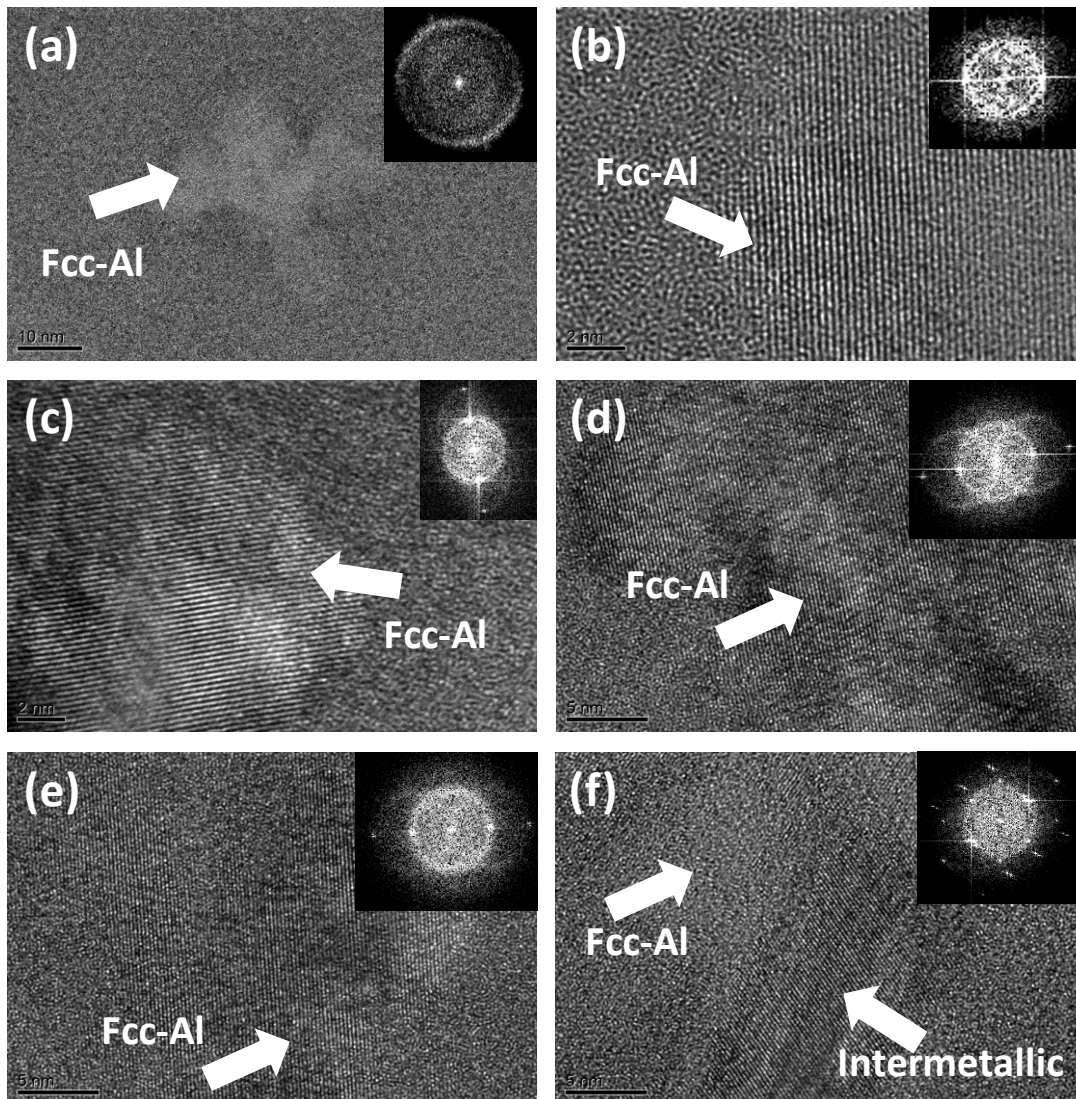
Figure 3.7. HRTEM images of (a) A, (b) B, (c) C, (d) D, (e) E and (f) F with FFT insets.

Figure 3.10(b) shows the differential Avrami exponent change with respect to crystallized fraction between 0-1 range. For the most part of the crystallization, n(x) stays around 2.5 after 100% crystallization it shows a steep increase. Such increase in the slope may be

attributed to a slowdown in the transformation process because of the soft impingement of the growing nanocrystals.
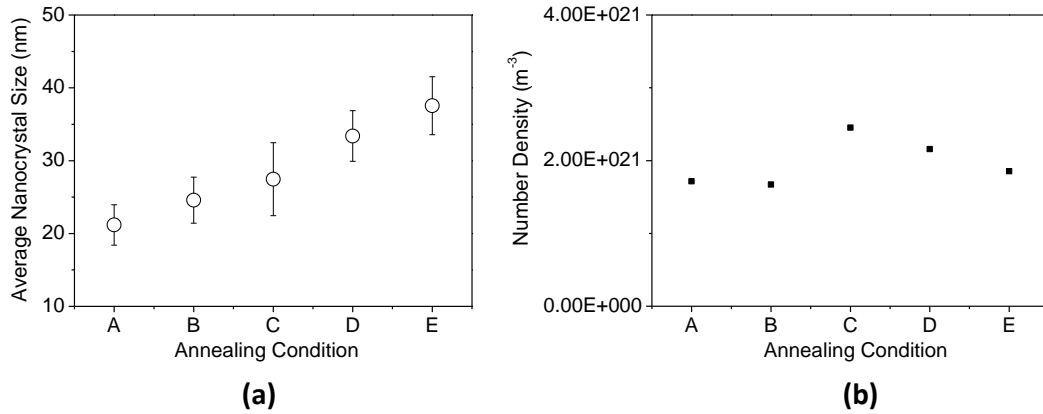
Figure 3.8. (a) The average size of nanocrystals and (b) volume number density of nanocrystals through the crystallization.
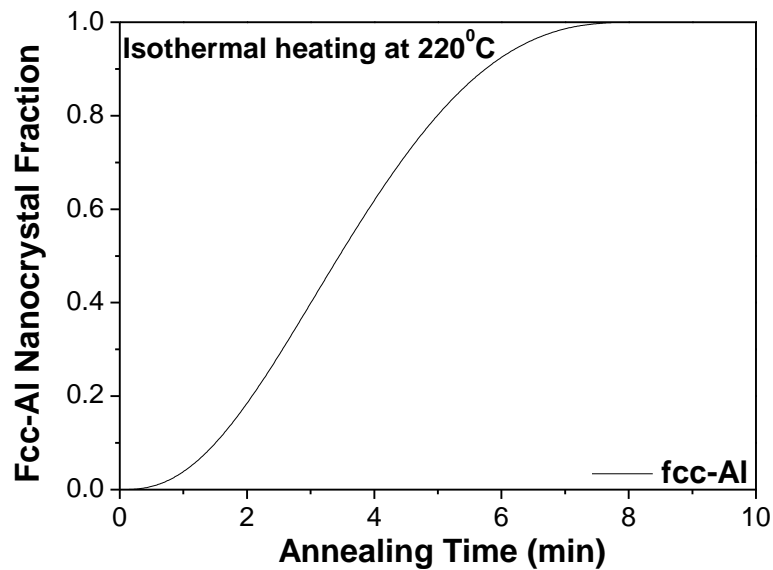
Figure 3.9. The crystallized fraction versus annealing time curve for fcc-Al crystallization.

Application of JMA is straightforward. On the other hand the results should be considered carefully. The Avrami exponent in our case indicates a three dimensional diffusion growth with constant nucleation rate. In three dimensional diffusional growths, particle grows with $\sqrt{t}$, where t is the annealing time [66]. This statement is in good agreement with our TEM observations. Figure 3.11 shows the change in average particle size with respect to $\sqrt{t}$.
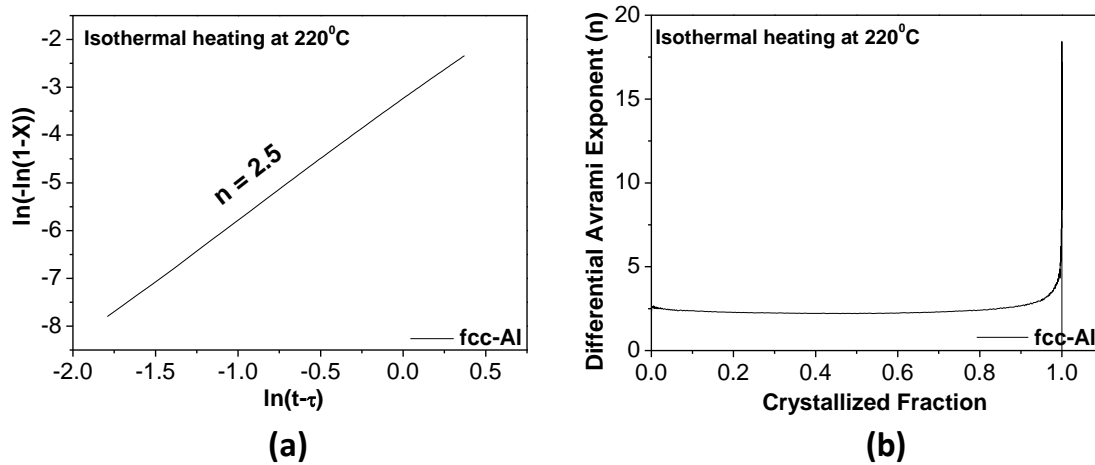
Figure 3.10. The JMA plot of (a) ln(-ln(1-x)) versus ln(t-r) for fcc-Al crystallization and (b) the derivative of JMA plot with respect to crystallized fraction.
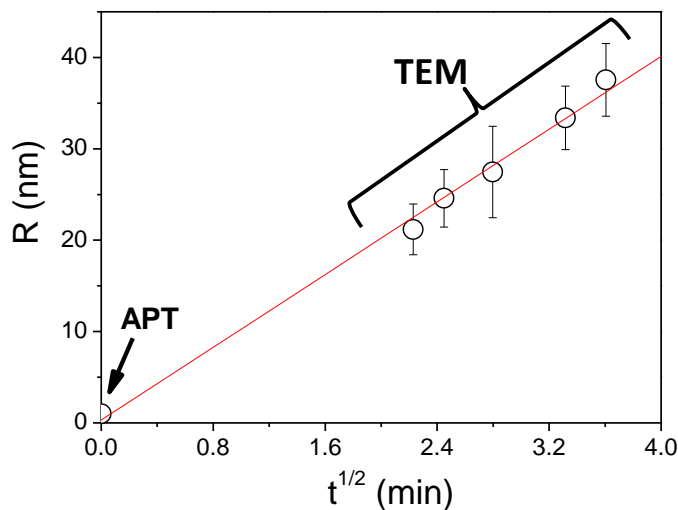
Figure 3.11. The average size versus t$^{1/2}$ curve for fcc-Al crystallization.

Average cluster size at 0 min is assumed to be 1 nm. This is coming from the previous work of Kalay et al. with atom probe tomography [26]. According to the results of that study, as-quenched alloy consists of isolated pure Al regions of 1-1.5 nm. The change in R with respect to $\sqrt{t}$ was perfectly fitted by a linear function (Figure 3.11). Therefore both Avrami and microstructural investigations indicated a diffusional type of growth in 3D. On the other hand there is clear conflict on the nucleation mechanism between the Avrami analyses and the observation. JMA predicts a constant nucleation rate where the number density of nuclei should be linearly increased with annealing time [37]. However, according to TEM and HRTEM analyses this value is close to be constant with time as shown in Figure 3.8(a). Furthermore if previous APT results are considered there is even an initial steady decrease

and then non-change in number density indicating zero nucleation rate. The possible reason for this discrepancy is much like related to the initial atomic configuration of amorphous alloy.

The existence of chemical and topological (MRO) separation in the as-quenched may affect the nucleation mechanism. JMA relies on the fact that precursor amorphous should be homogeneous. In our case it is more like a MRO + amorphous composite material. APT studies showed that initial nucleation takes place within these pure Al regions. Therefore initially an interface controlled mechanism may be active. The time scales considered for initial nucleation is extremely small. Therefore Avrami analyses derived from time-scale restricted DSC may fail to elucidate the details of nucleation mechanism. Further studies with state-of-art thermal and structural analyses instruments are required to come up with a reliable solution for nucleation mechanism.

3.4. Conclusion

Al-Tb amorphous alloys were devitrified under controlled temperature conditions. According to XRD and TEM analyses the first devitrification product is found to be of fcc-Al nanocrystals with high number of density. Crystallization kinetics were observed by JMA analyses using differential scanning calorimetry. JMA indicated a 3D diffusional growth with constant nucleation rate of fcc-Al nanocrystals on the other hand TEM, HRTEM and previous APT observations revealed a zero nucleation rate with diffusional growth. The major possible reason for the discrepancy between these results was related to initial non-homogeneous atomic configuration of as-quenched alloy. Fcc-Al preferential nucleate from the pure MRO Al regions disrupting the fundamental assumption of JMA. Further sophisticated analysis should be performed in smaller time scales in order to reveal the details of nucleation in marginal glass forming systems.

CHAPTER 4

MECHANICAL BEHAVIORS OF AMORPHOUS AND PARTIALLY DEVITRIFIED Al-Tb ALLOYS

4.1. Introduction

Al based metallic glasses have a greater potential to be used in aerospace application due to its lightweight high strength mechanical properties. However, mainly because of the localized stress along the shear bands, it is an elusive task to take full advantage of Al alloys in amorphous solid state. This chapter addresses some of the mechanical properties of Al glass formers in amorphous and partially devitrified states.

4.1.1 Deformation Mechanism in Metallic Glass

Plastic deformation is controlled by the slip systems in an ordinary crystalline structure [67-68]. Mechanism of slip systems depends on a parallel movement of two crystal regions that are related to each other by crystallographic planes. Slip system can be simply defined as the co-operation of the plane and the direction existing in a plane along which slip occurs [69]. On the other hand, the lack of long range crystal symmetry prevents the formation of any slip system for an amorphous structure. The limited plasticity observed in disorder systems is represented by so-called shear transformation zones (STZ) as firstly proposed by Argon [70]. STZ composed of a few hundreds of atoms and it act as shear stress riser during any deformation [11, 70]. The schematic representation of a slip system in crystals and STZ in amorphous structures is given in Figure 4.1.

The required activation energy and volume for shear transformation is significantly more than that for dislocation movement in crystals [11, 72]. This fact cause STZ become immobile so metallic glasses commonly require higher stress for yielding. Unfortunately the increase in yield strength does not compensate with an improvement in elasticity. Localization of plastic deformation over linked STZs occurs very quickly along a narrow path which results in catastrophic type of failure [11]. Introducing nanocrystals into the amorphous phase greatly improves the ductility of the materials [72, 73]. However, a fundamental understanding of the effects of nanocrystallization embedded in amorphous matrix to the mechanical properties is still unpuzzled. Further comprehensive studies are definitely needed to get a solid description and accurate scientific imports.
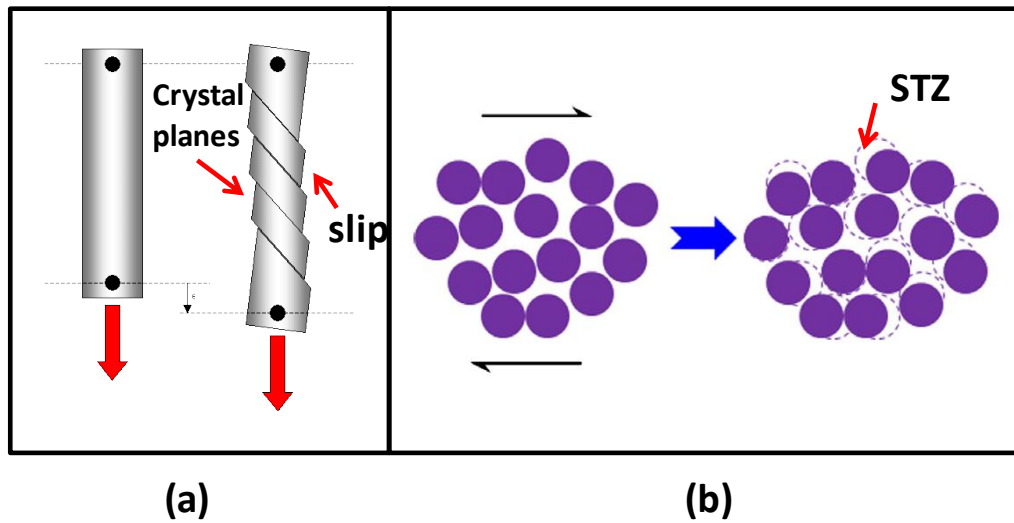
4.1 Schematic view of (a) slip system adopted from [71] and (b) STZ adopted from [11].

4.1.2 Mechanical Properties of Al-RE Marginal Glass Formers

The literature on mechanical properties of Al-based marginal glass formers is quite limited because of the practical difficulties in Al-based bulk metallic glass production. The required cooling rate is on the order of 10^6 K/s which limit the shape to be in ribbon form.

Tensile tests from ribbon specimens are not quite reliable but still give an idea on the fracture behavior. As it was stated in Chapter 1, Inoue et al. concluded that independent from atomic number, the tensile strength and the hardness of Al-RE was found to increase with RE content [4, 74]. In another study of same research group [73], fracture strength and strain of Al based amorphous alloys were compared. Figure 4.2 demonstrates the schematic views of different amorphous/nanocrystalline composites namely as (i) single amorphous phase, (ii) fcc-Al and intermetallic compound nanocrystalline phases, (iii) amorphous matrix with just fcc-Al nanoparticles, (iv) nanoscaled quasicrystalline particles surrounded by Al phase, (v) granular Al and amorphous phases at nanoscale and (vi) amorphous network including granular Al nanoparticles. The tested Al metallic glasses are in ribbon form. Among these stated conditions, fcc-Al nanoparticles having 3-5 nm in size and embedded in amorphous matrix gave the highest fracture strength being equal to 1560 MPa. This value is well beyond the ultimate tensile strength of AA2024 (470 MPa) and Al-Lithium 2195 alloy (720 MPa) which are highly used in aerospace applications. Minimum strength and elongation was found in alloys containing intermetallics. It is a very common observation that having intermetallic compounds greatly increases the brittleness and reduces the ductility [75].
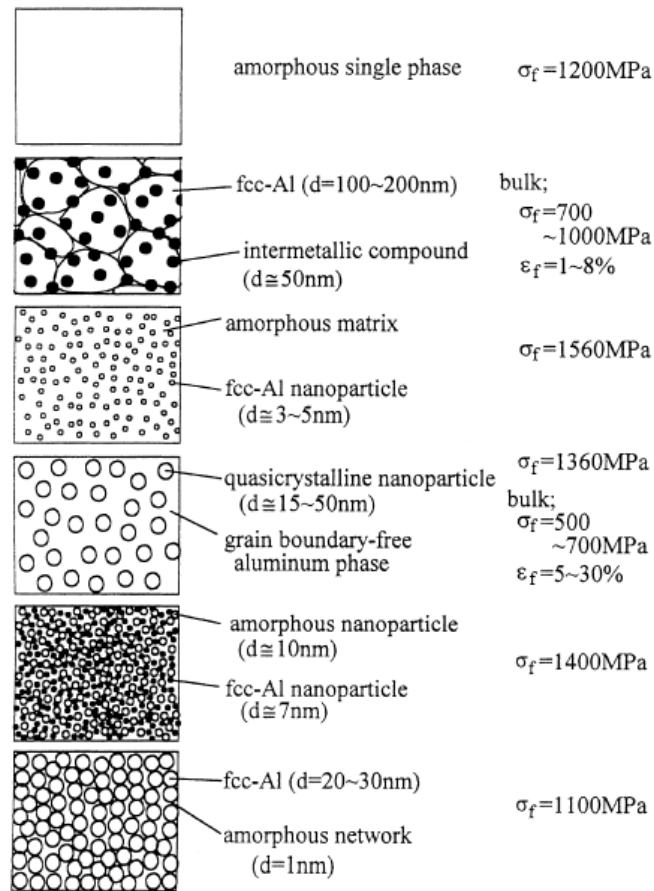
Figure 4.2 Mechanical properties of Al-based amorphous/crystal composites. Adopted from [73].

4.2. Experimental Procedure

Al$_{90}$Tb$_{10}$ ribbons were produced as explained in section 2.3.1

4.2.1 Controlled Devitrification of Specimens

Devitrification of amorphous samples was performed in oil bath to obtain nanocrystalline/amorphous composite materials. The procedure was previously explained in section 3.2.2. The process was repeated for three fcc-Al crystalline states (A, C, E), and an additional F condition to include the intermetallic compound. The annealing time and corresponding fcc-Al crystallization percentages (based on DSC) were given in Table 4.1.

Table 4.1 Annealing time and fcc-Al crystallization percentages of all states based on isothermal DSC data at 220^{0}C with average nanocrystal size.

Specimen	Annealing Time (sec.)	Fcc-Al Crystallization (%)	Nanocrystal Size (nm)
Amorphous	-	0	0
A	298	0.002%	21 ± 3
C	469	37%	28 ± 5
E	785	~100%	38 ± 4
F	1270	Second phase formed	54 ± 13

4.2.2 Hardness Tests

The samples were subjected to the micro-hardness test for the investigation of hardness changes from amorphous phase through the different levels of crystallization. Analyses were held with SHIMADZU HMV Micro Hardness Tester. Vickers hardness test conducted under a load of 980.7 mN (H$_v$ 0.1) for 10 seconds of dwell time. Ribbons were attached on a bulk aluminum plate having average hardness value of 154 H$_v$. Seven significant indentations were taken into account. In order to eliminate the errors potentially coming from the Al substrate, hardness tests were repeated on a steel plate having an average hardness of 354 H$_v$. Hardness values were collected from both air and wheel sides of each specimen.

4.2.3 Tensile Tests

A standard test procedure for metallic glass ribbons is missing. The common practice is to test the ribbons as they are casted from the melt-spinning. In our tests, we have adopted the procedures from metallic foil standards [76] and another previous work performed with melt-spun TiNi alloys [15, 77]. The specimen conditions were summarized in Table 4.2. Tension tests were held with 0.1 mm/min strain rate under 2N load by using Instron 5565 A testing machine. To prevent the tearing, grinding papers were inserted between the serrated wedges and specimen from both ends. The average thickness of the ribbons tested in tension is around 23 μm. The gage and overall lengths are 1 and 5 cm, respectively. Width of specimens was determined by micrometer and tabulated in Table 4.2

Table 4.2 Specimen dimensions for tensile test.

Sample Type	Specimen Width (mm)			
	1	**2**	**3**	**4**
Amorphous	1.8	1.6	1.6	1.6
A	1.5	1.4	1.7	1.4
C	1.5	1.3	1.4	1.4
E	1.4	1.5	1.5	1.8
F	1.4	1.5	0.8	1.0

4.2.4 Fracture Surface Analysis

The fractured surfaces after the tensile test were investigated by SEM. Specimens were attached perpendicular along the length so that a direct view of the surfaces can be obtained.

4.3. Results and Discussion

Tensile test results are given in Figure 4.3. The curves belong to most representing specimen in their group. The results are also tabulated in Table 4.3. The representative specimens were chosen according to test conditions. The selected ones are the specimens fractured close to middle region and showed no tearing. The overall results coming from all tests are given in Appendix 2.
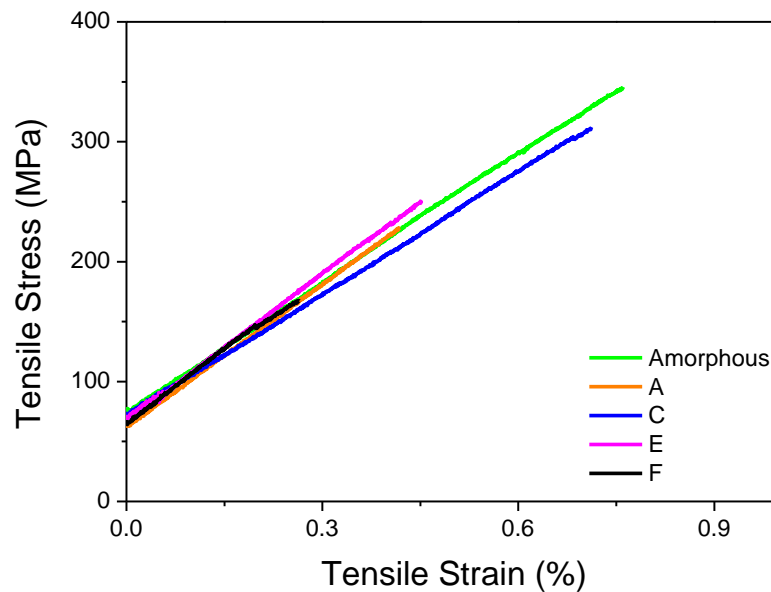
Figure 4.3 Tensile stress-strain diagrams of selected samples from five different conditions.

In line with the previous studies in literature, the tensile test results are quite chaotic because of the ribbon geometry used in measurements. All of the specimens fractured before considerable plastic deformation, so very little ductility was observed. As it is expected, the specimen having intermetallics showed the weakest strength and ductility. If the large aspect ratio of intermetallic phases (Figure 4.4) observed in this study is considered, having low strengthened ductility sounds reasonable. The highest strengths are observed for amorphous and C specimens. Specimen C has approximately 37% of nanocrystal according to DSC. Therefore it can be considered as an amorphous/nanocrystal composite. It is interesting to note that amorphous specimens have considerable amount of strength and strain at fracture point.

Table 4.3 Fracture stress and strain data of selected specimens.

Annealing State	Specimen Code	Stress at Fracture (Mpa)	Strain at Fracture (%)
AMORPHOUS	3	345.6	0.761
A	4	228.1	0.419
C	2	312.1	0.712
E	2	251.1	0.452
F	1	167.5	0.264
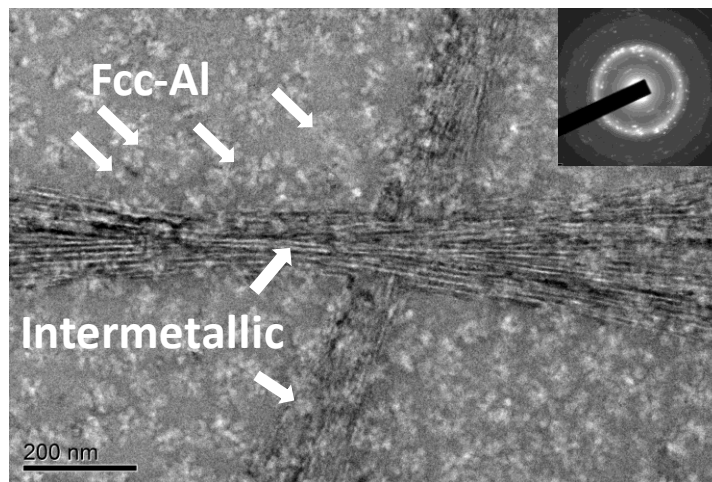
Figure 4.4 BF micrograph of state F, showing intermetallic phase and fcc-Al nanocrystals embedded in amorphous matrix. Inset shows the corresponding SAED.

The possible reason for having high strength in amorphous state is left out since it is out of the scope of this thesis. However, it definitely deserves future interest. A potential ground for having relatively high strength/strain might be related to MRO present in the amorphous matrix. Rather than having a fully disorder configuration, MRO structure may trigger the mobility of relatively long range ordered clusters (1-3nm) which results in an increase in strain. However, further critical mechanical testing and corresponding microstructural investigations should be performed by using relatively thicker specimens before drawing a solid conclusion. Because of thin ribbon shape of specimen, it is difficult to come with a significant conclusion on tensile test results.

Ribbon specimens are quite suitable to conduct micro hardness tests. The specimens were subjected to micro hardness tests from both sides on Al and steel blocks. The test results for Al and steel blocks are given in Figure 4.5 and Figure 4.6, respectively. The average hardness values are close to each other. This indicates ribbons have sufficient thickness so that effects of substrate in hardness measurement is minor. The wheel side of the ribbon showed a relatively higher hardness as compared to air side. This is quite typical since the level of vitrification on whell side, which touches and solidifies first during ejection of liquid onto

copper wheel, is expected to be higher. This can be seen by the dynamical increase in hardness values as well. For the same duration of annealing wheel side nanocrystallize and gets harder faster that the air side. For example for annealing condition A on Al substrate, wheel side has an average volue of 250 H_v on the other hand air side has an average of   190 H_v. After the specimens are fully nanocrystallized air and wheel side have similar values of hardness. Under fully nanocrystalline condition (E), hardness is increased to its 1.5 of original value. It is interesting to note that the critical aerospace material AA2024 has ultimate hardness values of 150H_v and 195H_v after peak-aged and equal channel angular pressing (ECAP) process [78]. In our case, nanocrystalline ribbons show a much higher hardness values indicating the potential strength of these materials. However, as it was mentioned previously, this type of nanocrystal and amorphous composite materials suffer from low plasticity. Therefore future studies on this field should be directed to find potential solutions to increase the ductility.
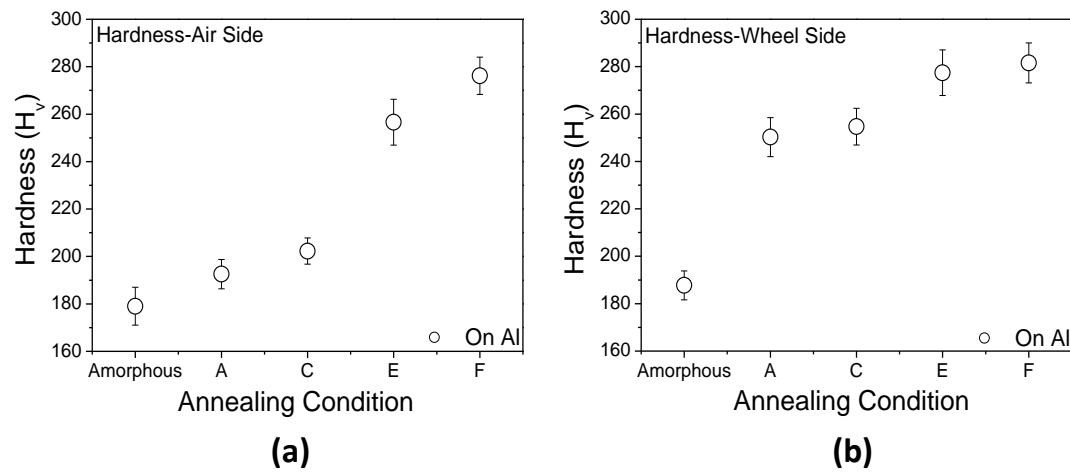
Figure 4.5 Hardness values (measured on a base sample of Al) of amorphous and all other crystallization states.

The brittle nature of the specimen can be also seen from fractographic analyses under SEM. None of specimen showed dimples indicating a ductile type of fracture. In amorphous specimen, tiny shear bands parallel to each other were detected (Figure 4.7). As it was stated before these shear bands are responsible for the catastrophic failures in metallic glass systems. As the specimens crystallized, multiplication and branching of shear bands occur (Figure 4.8). It seems that nanocrystals present in the annealed specimens cause the deflection of shear bands propagating in the amorphous matrix. In a previous study with Cu-Zr [79] it was argued that such multiplication of shear bands may enhance the plasticity.

In our study we have not observed a great deal of increase in plasticity despite the multiplication of shear bands after crystallization. As a matter of fact amorphous alloy showed relatively high strain values. However two facts need to be considered. First of all, specimen geometry is not suitable for tensile testing. Therefore some future work is needed to produce nanocrystal / amorphous composites in bulk geometry. Secondly, under the light

of the second and third chapters we think that the as-quenched alloys are not fully glassy but contain some MRO structures (1-3nm). On the microscopic levels reached by SEM shear bands may be seen continuous and single however on the atomic levels these MRO structure may cause deflection of shear band propagation leading a pseudo increase in plasticity. Therefore although it sounds speculative for now, the relatively high level of strain in as-quenched state may be intrinsic rather than an anomaly because of the specimen geometry. This definitely requires further tensile test analyses and critical TEM investigations.
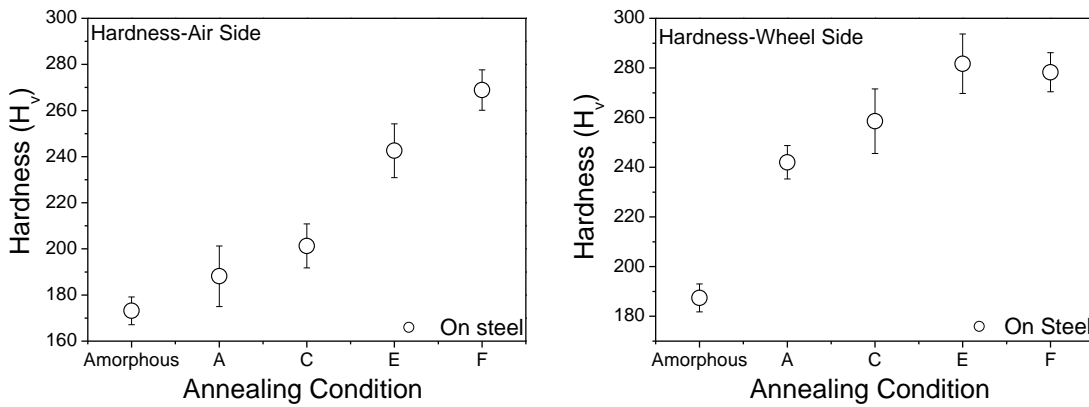
Figure 4.6 Hardness values (measured on a base sample of steel) of amorphous and all other crystallization states.
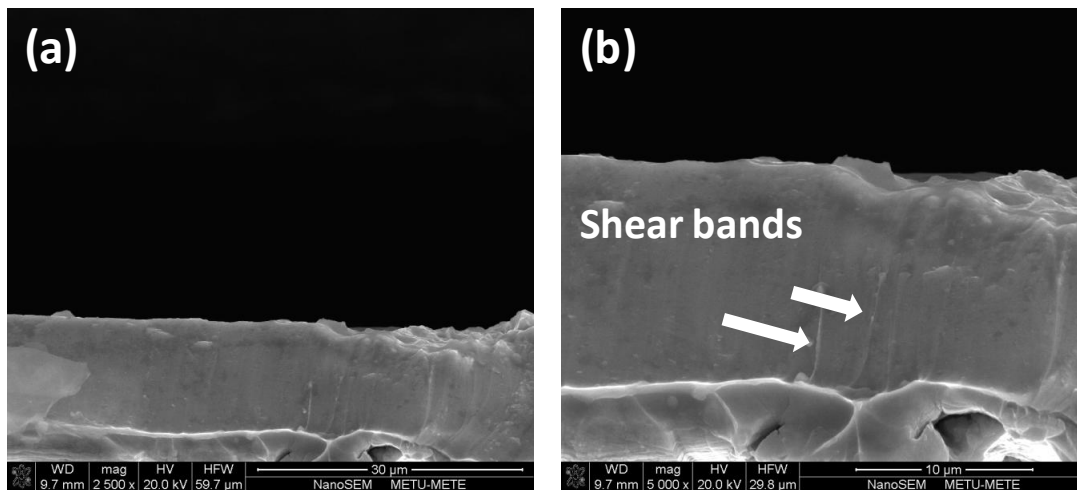
Figure 4.7 SEM micrographs showing fracture surfaces of amorphous state under two different magnification: (a) 2500x and (b) 5000x respectively.
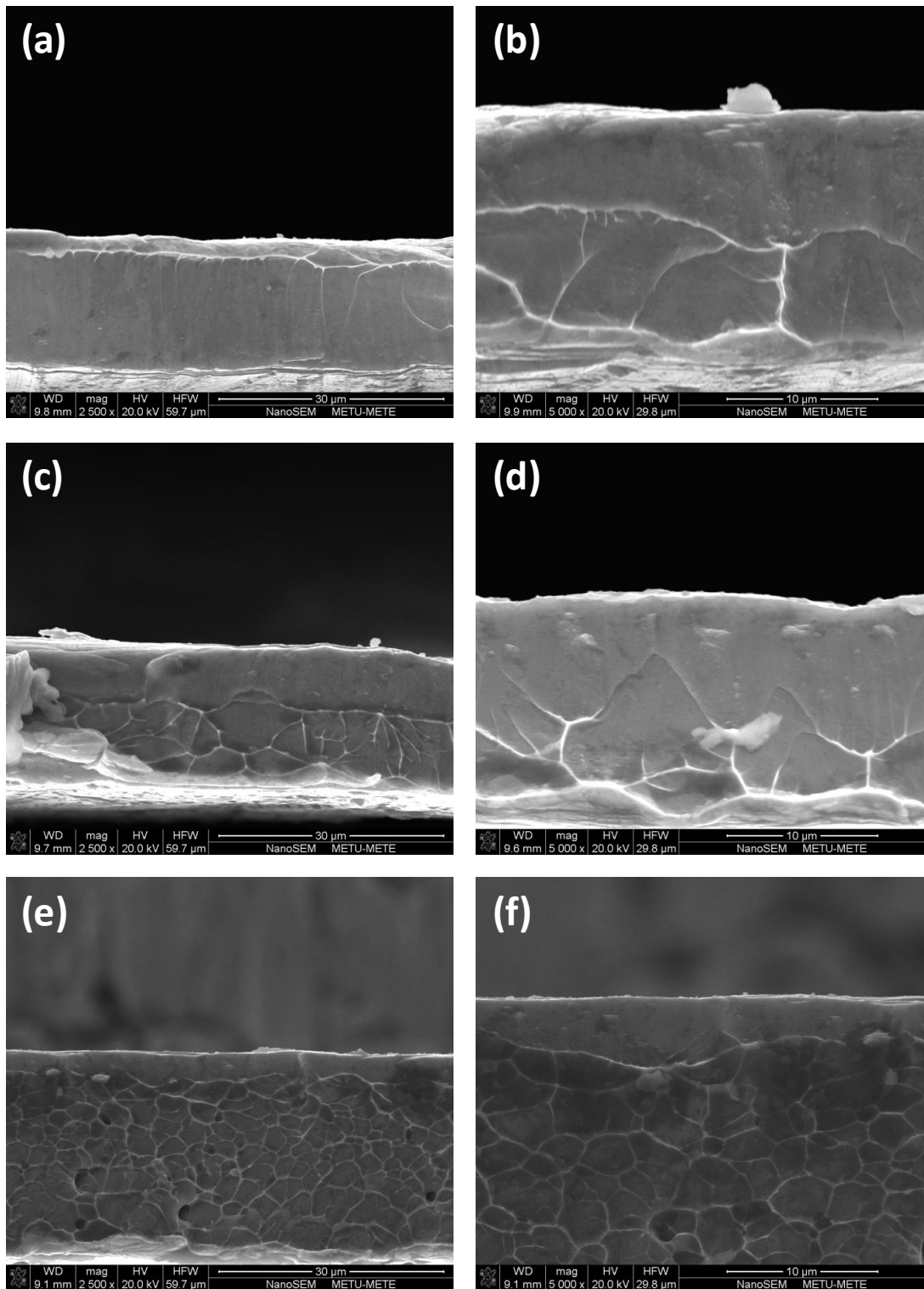
Figure 4.8 SEM micrographs showing fracture surfaces of crystallized states A, C and E under two different magnification: 2500x and 5000x respectively.

4.4. Conclusion

As-quenched specimens of $Al_{90}Tb_{10}$ ribbons were devitrified to different levels of nanocrystal populations and size. The tensile test results indicated a brittle type of failure for all specimens. Specimens with the needle like intermetallics gave the weakest results. The as-quenched and 37% nanocrystal specimens showed relatively high tensile strength. Hardness values were found to increase with annealing time as it is expected. The maximum reachable hardness values are higher as compared to popular Al alloys used in aerospace engineering. The failure analyses by SEM indicated multiplication and branching of shear bands responsible for the brittleness. Future studies are required to derive the mutual interactions of shear band propagation and nanocrystal formation in alloys with amorphous precursor.

CHAPTER 5

CONCLUSION AND FUTURE RECOMMENDATIONS

5.1. Conclusion

In this thesis study, structural order hidden in amorphous and liquid states of Al-Tb alloy and the nanocrystallization mechanism during annealing were investigated and various critical mechanical behaviors were determined.

In first part of the study, the structure of solid amorphous and liquid was investigated in details. Promising medium range ordered clusters were detected by RMC simulation from synchrotron X-ray diffraction experiments. It seems that MRO existed in solid amorphous state also persists to exist in molten state. The experimental findings are perfectly in good agreement with atomic simulations. The Warren-Cowley type analysis indicated regions of pure Al with an average size of 1-2 nms.

In the second part of the study, the as-spun ribbons were devitrified and the crystallization mechanism was monitored during isothermal heating. The morphology, number density and size of the nanocrystals were determined by critical TEM and HRTEM experiments. Crystallization kinetics was also determined by well-known JMA approach. The nucleation and growth mechanisms calculated by JMA and observed with TEM were not in good agreement. It was clearly observed that the number density reached at the beginning of the crystallization remained the same through the whole crystallization process. JMA seems to contradict with that statement. The discrepancy between JMA and experimental observations were explained with the presence of MRO in the amorphous structure. The results of this study also points out that the popular JMA approach should be considered carefully in order to reveal the crystallization kinetics of metallic glass former alloys.

In the last part of the study, mechanical properties of the as-quenched and nanocrystallized alloys were taken under investigation. Tensile tests were conducted from ribbon specimens. The as-quenched and half-nanocrystallized specimens showed the better mechanical properties. Ribbons with intermetallic formation failed at relatively low stress as it was expected. Unfortunately geometry of the ribbons is not suitable to derive a solid conclusion on tensile properties. On the other hand, hardness measurements were quite consistent and kept increasing with the increase in nanocrystal percent. Fracture surfaces of the tensile specimens were analyzed under SEM. Shear bands were found to exist in amorphous

specimens and they were observed to be multiplied and branched with the introducing nanocrystals into the matrix during isothermal hold.

5.2. Future Recommendations

The origin of high number density of nuclei formation is still an enigma. Further state of the art experiments and stronger atomistic models should be implemented. Different alloy systems can be checked to see if similar behaviors are observed.

In order to get a solid proof of the existence of longer correlations in the molten state special experimental set-ups (i.e. levitation melting) can be built to reach higher temperatures without contamination or holder-specimen interaction. Another way to prove the MRO is to alter the production pathway. For example if MRO is originated from liquid state; if one can suppress the liquid formation but still gets the amorphous solid, we should not expect to observe any MRO. Such pathways can be created with magnetron sputtering or mechanical milling techniques to prove the current hypothesis. Mechanical features definitely deserve further attention due to the lightweight high strength properties of Al-based alloys. The disability of producing bulk metallic Al-RE prevents conducting successful mechanical tests. The effect of MRO in shear band propagation is another topic that can be considered as a future study.

REFERENCES

[1]   Klement W., Williens R.H., Duwez P., Non-crystalline structure in solidified gold-silicon alloys, Nature 187 (1960) pp. 869 – 70.

[2]   Duwez P., Williens R.H., Klement W., Continuous series of metastable solid solutions in silver-copper alloys, J. Appl. Phys. 31 (1960) pp. 1136 – 1137.

[3]   Egami T., Magnetic amorphous alloys: physics and technological applications, Rep. Prog. Phys. 47 (1984) pp. 1601 – 1725.

[4]   Inoue A., Amorphous, nanoquasicrystalline and nanocrsytalline alloys in Al-based systems, Prog. Mater. Sci. 43 (1998) pp. 365 – 520.

[5]   Gorant J., Liquid golf, Popular Mechanics 175 (1998) pp. 30

[6]   Johnson W.L., Fundamental aspects of bulk metallic glass formation in multicomponent alloys, Mater. Sci. Forum 225-227 (1996) pp.35 – 50.

[7]   Glassy Steel, ORNL Review 38 (2005)

[8]   Ponnambalam V., Poon S.J., Fe-based bulk metallic glasses with diameter thickness larger than one centimeter, J. Mater. Res. 19 (2004) pp. 1320 – 1323.

[9]   Busch R., Bakke E., Johnson W.L., Viscosity of the supercooled liquid and relaxation at the glass transition of the $Zr_{46.75}Ti_{8.25}Cu_{7.5}Ni_{10}Be_{27.5}$ bulk metallic glass forming alloy, Acta Mater. 46 (1998) pp. 4725 – 4732.

[10]   Battezzati L., Pozzovivo S., Rizzi P., Nanocrystalline aluminum alloys, ENN 6 (2004) pp. 341 – 364.

[11]   Cheng Y.Q., Ma E., Atomic-level structure and structure-property relationship in metallic glasses, Prog. Mater. Sci. 56 (2011) pp. 379 – 473.

[12]   Löffler J.F., Bulk metallic glasses, Intermetallics 11 (2003) pp. 529 – 540.

[13]   Inoue A., Stabilization of metallic supercooled liquid and bulk amorphous alloys, Acta Mater. 48 (2000) pp. 279 – 306.

[14]   Kulik T., Nanocrystallization of metallic glasses, J. Non-Cryst. Solids 287 (2001) pp. 145 – 161.

[15]   Mehrabi K., Bruncko M., Mackay B.J., Kneissl A.C., Influence of quenching rates on equiatomic NiTi ribbons fabricated by melt-spinning, J. Mater. Eng. Perform. 18 (2009) pp. 475 – 478.

[16]   Miracle D.B., A structural model for metallic glasses, Nat. Mater. 3 (2004) pp. 697 – 702.

[17]   Egami T., Billinge S.J.L., Underneath the Bragg Peaks Structural Analysis of Complex Materials, Elsevier 2003

[18]   Sheng H.W., Cheng Y.Q., Lee P.L., Shastri S.D., Ma E, Atomic packing in multicomponent aluminum-based metallic glasses, Acta Mater 56 (2008) pp. 6264 – 6272.

[19]   Feigin L.A., Svergun D.I., Structure analysis by small-angle X-ray and neutron scattering, New York: Plenum Press 1987

[20]   Pecharsky V.K., Zavalij P.Y., Fundamentals of powder diffraction and structural characterization of materials, Springer Science + Business Media, Inc. 2005

[21]   Kalay Y.E., Chumbley L.S., Anderson I.E., Characterization of a marginal glass former alloy solidified in gas atomized powders, Mater. Sci. Eng. A 490 (2008) pp. 72 – 80.

[22]   Kalay Y.E., Yeager C., Chumbley L.S., Kramer M.J., Anderson I.E., Initial crystallization in a nanostructured Al-Sm rare earth alloy, J. Non-Cryst. Solids 356 (2010) pp. 1416 – 1424.

[23]   Wilde G., Sieber H., Perepezko JH., Glass formation versus nanocrystallization in an $Al_{92}Sm_8$ alloy, Scripta Mater. 40 (1999) pp. 779 – 783.

[24]   Treacy M.M.J., Gibson J.M., Fan L., Paterson D.J., McNulty I., Fluctuation microscopy: a probe of medium range order, Rep. Prog. Phys. 68 (2005) pp. 2899 – 2944.

[25]   Miller M.K., Forbes R.G., Atom probe tomography, Mater. Charact. 60 (2009) pp. 461 – 469.

[26]   Kalay Y.E., Kalay I., Hwang J., Voyles P.M., Kramer M.J., Local chemical and topological order in Al-Tb and its role in controlling nanocrystal formation, Acta Mater. 60 (2012) pp. 994 – 1003.

[27]   Kalay Y.E., Chumbley S., Anderson I.E., Crystallizatin behaviour in highly driven marginal glass forming alloy, J. Non-Cryst. Solids 354 (2008) pp. 3040 – 3048.

[28]   Kresse G., Joubert D,, From ultrasoft pseudopotentials to the projector augmented-wave method, Phys. Rev. B 59 (1999) pp. 1758 – 1775.

[29]   Kresse G., Hafner J., Ab-initio molecular-dynamics for liquid-metals, Phys. Rev. B 47 (1993) pp. 558 – 561.

[30]   Kresse G., Furthmüller J., Efficient iterative schemes for ab-initio total-energy calculations using a plane-wave basis set, Phys. Rev. B 54 (1996) pp. 11169 – 11186.

[31]   Kresse G., Furthmüller J., Efficiency of ab-initio total energy calculations for metals and semiconductors using a plane-wave basis set, Comput. Mater. Sci. 6 (1996) pp. 15 – 50.

[32]   McGreevy R.L., Reverse Monte Carlo modeling, J. Phys–Condense Matter 13 (2001) pp. 877 – 913.

[33]   Kalay Y.E., Chumbley L.S., Kramer M.J., Anderson I.E., Local structure in marginal glass forming Al-Sm alloy, Intermetallics 18 (2010) pp. 1676 – 1682.

[34]   Honeycutt J.D., Andersen H.C., molecular dynamics study of melting and freezing of small Lennard-Jones clusters, J. Phys. Chem. 91 (1987) pp. 4950 – 4963.

[35]   Warren B.E., X-ray diffraction, Dover Publications Inc., New York 1990

[36]   Cowley J.M., X-Ray measurement of order in single crystals of Cu_3Au, J. Appl. Phys. 21 (1950) pp. 24 – 29.

[37]   Fivez J., Longuemart S., Glorieux C., Fragility of supercooled liquids from differential scanning calorimetry traces: theory and experiment, J. Chem. Phys. 136 (2012) pp. 044502-(1 – 9).

[38]   Louzguine-Luzgin D.V., Inoue A., Structure and transformation behavior of a rapidly solidified Al-Y-Ni-Co-Pd alloy, J. Alloy. Compd. 399 (2005) pp. 78 – 85.

[39]   Jin L., Kang Y.B., Chartrand P., Fuerst C.D., Thermodynamic evaluation and optimization of Al-Gd, Al-Tb, Al-Dy, Al-Ho and Al-Er systems using a modified quasichemical model for the liquid, CALPHAD 34 (2010) pp. 456 – 466.

[40]   Perepezko J.H., Hebert R.J., Wu R.I., Wilde G., Primary crystallization in amorphous Al-based alloys, J. Non-Cryst. Solids 317 (2003) pp. 52– 61.

[41]   Kelton K.F., Miller M.K., Sahu K.K., Mauro N. A., Longsreth L. -Spoor, Saha D., Nussinov Z., Phase separation mediated devitrification of $Al_{88}Y_7Fe_5$ glasses, Acta Mater. 58 (2010) pp. 4199 – 4206.

[42]   Gangopadhyay A.K., Croat T.K., Kelton K.F., The effect of phase separation on subsequent crystallization in $Al_{88}Gd_6La_2Ni_4$, Acta Mater. 48 (2000) pp. 4035 – 4043.

[43]   Chu J.P., Wang C.Y., Chen L.J., Chen Q., Annealing-induced amorphization in a sputtered glass-forming film: In-situ transmission electron microscopy observation, Surf. Coat. Tech. 205 (2011) pp. 2914 – 2918.

[44] Gao M.C., Guo F., Poon S.J., Shiflet G.J., Development of fcc-Al nanocrystals in Al-Ni-Gd metallic glasses during continuous heating DSC scan, Mater. Sci. Eng. A 485 (2008) pp. 532 – 543.

[45] He Y., Poon S.J., Shiflet G.J., Synthesis and properties of metallic glasses that contain aluminum, Science 241 (1988) pp. 1640 – 1642.

[46] Stratton W.G., Hamann J., Perepezko J.H., Voyles P.M., Aluminum nanoscale order in amorphous $Al_{92}Sm_8$ measured by fluctuation electron microcopy, Appl. Phys. Lett. 86 (2005) pp. 1419101 – 1419103.

[47] Fang X.W., Wang C.Z., Yao Y.X., Ding Z.J., Ho K.M., Signature of $Al_{11}Sm_3$ fragments in undercooled $Al_{90}Sm_{10}$ liquid from ab-initio molecular dynamics simulations, J. Phys.: Condens. Matter 23 (2011) pp. 2351041 – 2351047.

[48] Perepezko J.H., Hebert R.J., Tong W.S., Amorphization and nanostructure synthesis in Al alloys, Intermetallics 10 (2002) pp. 1079 – 1088.

[49] Materials Preparation Center, A.L., US DOE Basic Energy Sciences, Ames, IA, USA, http://www.ameslab.gov/mpc. (Last visited on: 17.02.2013)

[50] Hwang J., Malgarejo Z.H., Kalay Y.E., Kalay I., Kramer M. J., Stone D. S., Voyles P. M., Nanoscale structure and structural relaxation in $Zr_{50}Cu_{45}A_{l5}$ bulk metallic glass, Phys. Rev. Lett. 108 (2012) pp. 1955051 – 1955055.

[51] Elliott S.R., Medium-range structural order in covalent amorphous solids, Nature 354 (1991) pp. 445 – 452.

[52] Jingyu Q., Xiufang B., Sliusarenko S.I., Weimin W., Pre-peak in the structure factor of liquid Al-Fe alloy, J. Phys.: Condens. Matter. 10 (1998) pp. 1211 – 1218.

[53] Cheng Y.Q., Sheng H.W., Ma E., Relationship between structure, dynamics and mechanical properties in metallic glass-forming alloys, Phys. Rev. B 78 (2008) pp. 014207-(1 – 7).

[54] Kelton K.F., Time-dependent nucleation in partitioning transformations, Acta Mater. 48 (2000) pp. 1967 – 1980.

[55] Tian N., Ohnuma M., Ohkubo T., Hono K., Primary crystallization of an $Al_{88}Gd_6Er_2Ni_4$ metallic glass, Mater. Trans. JIM 46 (2005) pp. 2880 – 2885.

[56] Li Q., Johnson E., Johansen A., Sharlot-Kristensen L., On glass formation in rapidly solidified aluminum-based alloys, J. Mater. Res. 7, (1992) pp. 2756 – 2764.

[57]   Christian J.W., The Theory of Transformation in Metals and Alloys, Pergamon Press, Oxford, 1975.

[58]   Avrami M., Granulation, phase change and microstructure kinetics of phase change III, J. Chem. Phys. 9 (1941) pp. 177 – 184.

[59]   Allen D.R., Foley J.C., Perepezko J.H., Nanocrystal development during primary crystallization of amorphous alloys, Acta Mater. 46 (1998) pp. 431 – 440.

[60]   Lay M.D.H., Hill A.J., Saksida P.G., Gibson M.A., Bastow T.J., Al NMR measurement of fcc Al configurations in as-quenched $Al_{85}Ni_{11}Y_4$ metallic glass and crystallization kinetics of Al nanocrystals, Acta Mater. 60 (2012) pp. 79 – 88.

[61]   Hebert R.J., Perepezko J.H., Effect of cold-rolling on the crystallization behavior of amorphous $Al_{88}Y_7Fe_5$ alloy, Mater. Sci. Eng. A 375 – 377 (2004) pp. 728 – 732.

[62]   Cahn J.W., Nutting J., Transmission quantitative metallography, Trans. Met. Soc. A.I.M.E. 215 (1959) pp. 526 – 528.

[63]   Stratton W.G., Medium Range Order in High Aluminum Content Amorphous Alloys Measured by Fluctuation Electron Microscopy, Ph.D. Thesis, (2007) University of Wisconsin-Madison, pp. 51.

[64]   Freeman L.A., Howie A., Mistry A.B., Gaskell P.H., The structure of non-crystalline materials, Taylor and Francis, London, 1976.

[65]   Wang J., Kou H.C., Gu X.F., Li J.S., Xing L.Q., Hu R., Zhou L., On discussion of the applicability of local Avrami exponent: errors and solutions, Mater. Lett. 63 (2009) pp. 1153 – 1155.

[66]   Venkataraman S., Hermann H., Mickel C., Schultz L., Sordelet D.J., Eckert J., Calorimetric study of the crystallization kinetics of $Cu_{47}Ti_{33}Zr_{11}Ni_8Si_1$ metallic glass, Phys. Rev. B 75 (2007) pp. 104206-(1 – 9).

[67]   Louzguine-Luzgin D.V., Vinogradov A., Li S., Kawashima A., Xie G., Yavari A.R., Inoue A., Deformation and fracture behavior of metallic glassy alloys and glassy-crystal composites, Metal. Mater. Trans. A 42 (2011) pp. 1504 – 1510.

[68]   Takeuchi S., Edagawa K., Atomistic simulation and modeling of localized shear deformation in metallic glasses, Prog. Mater. Sci. 56 (2011) pp. 785 – 816.

[69]   Verhoeven J.D., Fundamentals of physical metallurgy, John Wiley & Sons, Inc. 1975

[70]   Argon A.S., Plastic deformation in metallic glasses, Acta Metall. 27 (1979) pp. 47 – 58.

[71]   University of Cambridge, "Dissemination of IT for the Promotion of Materials Science," http://www.doitpoms.ac.uk/tlplib/slip/images/diagram001.gif (Last visited on: 17.02.2013)

[72]   Pan D., Inoue A., Sakurai T., Chen M.W., Experimental characterization of shear transformation zones for plastic flow of bulk metallic glasses, Proc. Natl. Acad. Sci. USA 105 (2008) pp. 14769 – 17772.

[73]   Inoue A., Kimura H., Fabrications and mechanical properties of bulk amorphous, nanocrystalline, nanoquasicrystalline alloys in aluminum-based system, J. Light Met. 1 (2001) pp. 31 – 41.

[74]   Inoue A., Zhang T., Kita K., Masumoto T., Mechanical strengths, thermal stability and electrical resistivity of aluminum-rare earth metal binary amorphous alloys, Mater. Trans. JIM 30 (1989) pp. 870 – 877.

[75]   Liu C.T., Heatherly L., Easton D.S., Carmichael C.A., Schneibel J.H., Chen C.H., Wright J.L., Yoo M.H., Horton J.A., Inoue A, Test environments and mechanical properties of Zr-base bulk amorphous alloys, Metal. Mater. Trans. A 29A (1998) pp. 1811 – 1820.

[76]   Standard Test Methods of Tension Testing of Metallic Foil, ASTM International E 345 – 93 pp. 434 – 438.

[77]   Wu D., Crone W.C., Perepezko J., Mechanical behavior of nanostructured melt spun NiTi shape memory alloy, Soc. Exp. Mech. (2002).

[78]   Kotan G., Tan E., Kalay Y.E., Gür C.H., Homogenization of ECAPed Al 2024 alloy through age-hardening, Mater. Sci. Eng. A 559 (2013) pp. 601 – 606.

[79]   Lee S.W., Huh M.Y., Fleury E., Lee J.C., Crystallization-induced plasticity of Cu-Zr containing bulk amorphous alloys, Acta Mater. 54 (2006) pp. 349 – 355.
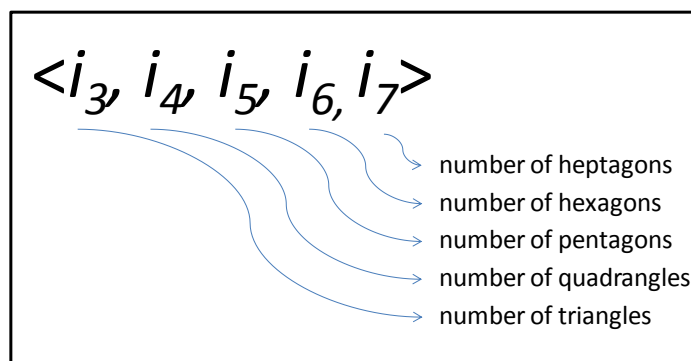
APPENDIX A

VORONOI TESSELLATION

Voronoi Tessellation divides the three dimensional space into cluster-like regions that centered by each atom in the structure. There exists a plane that created to divide all lines connecting the neighbor atoms to center atom into two parts and there becomes a section kept inside the inner plane. This section is named as a Voronoi cell which separates the closest neighbors of the center atom from all other atoms of the space [11]. A schematic distribution of a Voronoi cell, the nearest neighbors of the center atom (with common neighbor analysis (CNA) index) and a three dimensional Voronoi Tessellation is given in Figure 1.

(a)   **(b)**   **(c)**
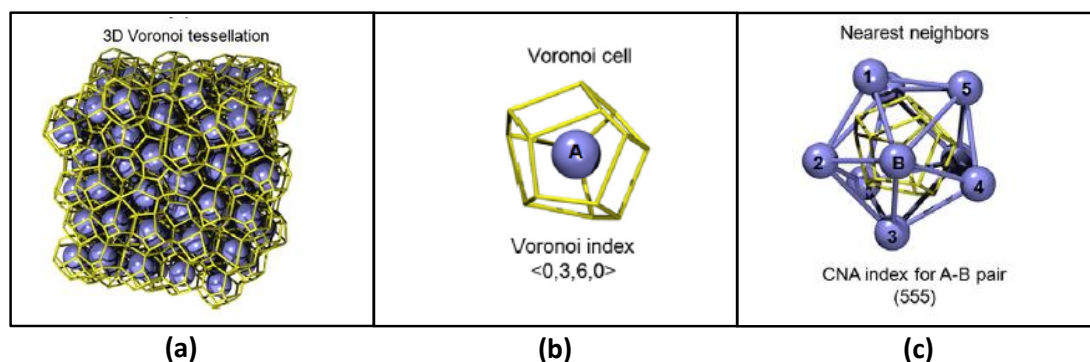
Figure 1. Schematic view of (a) Voronoi tessellation, (b) Voronoi cell of a center atom having three quadrangular faces and five pentagonal faces with an index of <0,3,6,0,0> and (c) a center atom with five common nearest neighbors. Adopted from [11].

In order to show the arrangements and symmetry of neighbor atoms around the center atom, the Voronoi index is used. Figure 2 shows a four number vector that gives the polygons on the Voronoi polyhedra.

$$<i_3, i_4, i_5, i_{6,} i_7>$$

- number of heptagons
- number of hexagons
- number of pentagons
- number of quadrangles
- number of triangles

Figure 2. Voronoi index example with a five number vector.

APPENDIX B

TENSILE TEST RESULTS

Table 1 Fracture stress and strain values for all mechanical tests.

Annealing State	Specimen Code Numb.	Stress at Fracture (MPa)	Strain at Fracture (%)	Failure Type
AMORPHOUS	1	260.0	0.488	Fractured close to grip
	2	314.0	0.543	Fractured close to grip
	3	345.6	0.761	OK
	4	299.0	0.775	OK
A	1	215.0	0.537	OK
	2	293.0	0.636	Torn
	3	244.0	0.515	Fractured close to grip
	4	228.1	0.419	OK
C	1	304.0	0.717	OK
	2	312.1	0.712	OK
	3	135.0	0.187	Fractured close to grip
E	1	102.0	0.058	Fractured close to grip
	2	251.1	0.452	OK
	3	211.0	0.589	Fractured close to grip
	4	129.0	0.401	Torn
	5	179.0	0.483	Torn
	6	247.6	0.588	OK
	7	270.0	0.656	Fractured close to grip
	8	157.0	0.293	Fractured close to grip
	9	186.0	0.263	Fractured close to grip
	10	54.0	0.028	Fractured close to grip
F	1	167.5	0.264	OK
	2	239.0	0.542	Torn
	3	228.0	0.428	Fractured close to grip
	4	393.0	0.802	Torn
	5	305.0	0.850	Torn